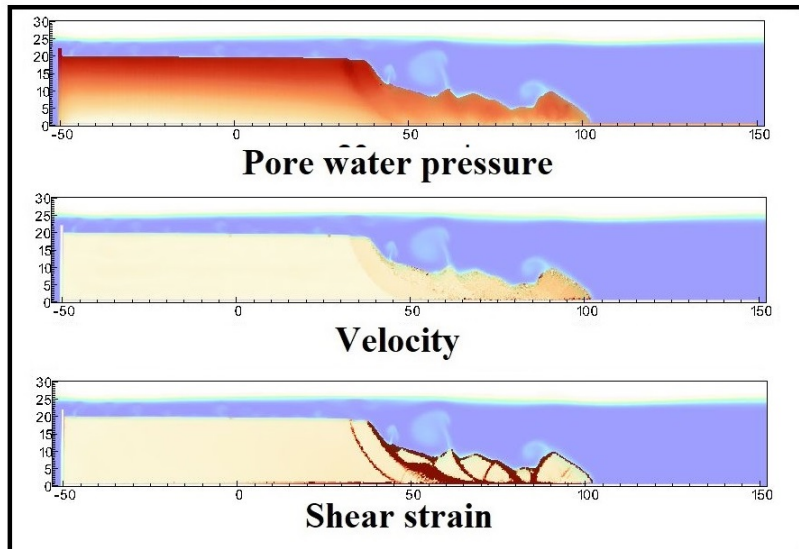


- 1 Graphical Abstract
- 2 MPMICE: A hybrid MPM-CFD model for simulating coupled problems in porous media. Application to earthquake-induced submarine landslides
- 3 Quoc Anh Tran, Gustav Grimstad, Seyed Ali Ghoreishian Amiri



**Application to earthquake-induced submarine landslide**

<sub>6</sub> Highlights

<sub>7</sub> **MPMICE: A hybrid MPM-CFD model for simulating coupled prob-**  
<sub>8</sub> **lems in porous media. Application to earthquake-induced subma-**  
<sub>9</sub> **rine landslides**

<sub>10</sub> Quoc Anh Tran, Gustav Grimstad, Seyed Ali Ghoreishian Amiri

- <sub>11</sub> • MPMICE is introduced for multiphase flow in porous media.
- <sub>12</sub> • Material Point method allows to model large deformation of non-isothermal  
<sub>13</sub> porous media.
- <sub>14</sub> • ICE (compressible multi-material CFD formulation) allows to stabilize  
<sub>15</sub> stabilizing pore water pressure and turbulent flow.
- <sub>16</sub> • MPMICE is validated and apply to simulate the earthquake-induced  
<sub>17</sub> submarine landslide.

<sup>18</sup> MPMICE: A hybrid MPM-CFD model for simulating  
<sup>19</sup> coupled problems in porous media. Application to  
<sup>20</sup> earthquake-induced submarine landslides

<sup>21</sup> Quoc Anh Tran<sup>a</sup>, Gustav Grimstad<sup>a</sup>, Seyed Ali Ghoreishian Amiri<sup>a</sup>

<sup>a</sup>*Norwegian University of Science and Technology, , Trondheim, 7034, Norway*

---

## <sup>22</sup> Abstract

<sup>23</sup> In this paper, we describe a soil-fluid-structure interaction model that com-  
<sup>24</sup> bines soil mechanics (saturated sediments), fluid mechanics (seawater or air),  
<sup>25</sup> and solid mechanics (structures). The formulation combines the Material  
<sup>26</sup> Point Method, which models large deformation of the porous media and the  
<sup>27</sup> structure, with the Implicit Continuous-fluid Eulerian, which models com-  
<sup>28</sup> plex fluid flows. We validate the model and simulate the whole process of  
<sup>29</sup> earthquake-induced submarine landslides. We show that this model captures  
<sup>30</sup> complex interactions between saturated sediment, seawater, and structure,  
<sup>31</sup> so we can use the model to estimate the impact of potential submarine land-  
<sup>32</sup> slides on offshore structures.

<sup>33</sup> *Keywords:*

<sup>34</sup> Material Point Method, MPMICE, submarine landslide.

---

35	<b>Contents</b>	
36	<b>Nomenclature</b>	4
37	<b>Introduction</b>	6
38	<b>Theory and formulation</b>	8
39	Assumptions . . . . .	8
40	Governing equations . . . . .	9
41	Constitutive soil model . . . . .	11
42	Turbulent model . . . . .	12
43	Frictional force for soil-structure interaction . . . . .	12
44	Momentum and Energy exchange model . . . . .	13
45	Solving momentum and energy exchange with an implicit solver	14
46	Equation of state for fluid phases . . . . .	16
47	<b>Numerical implementation</b>	17
48	Interpolation from Solid Particle to Grid . . . . .	18
49	Compute equation of state for fluid phase . . . . .	20
50	Compute face-centered velocity Compute cell face velocity . . . . .	20
51	Compute face-centered temperature Compute cell face temperature . . . . .	21
52	Compute fluid pressure (implicit scheme) . . . . .	22
53	Compute viscous shear stress term of the fluid phase . . . . .	22
54	Compute nodal internal temperature of the solid phase . . . . .	23
55	Compute and integrate acceleration of the solid phase . . . . .	23
56	Compute Lagrangian value (mass, momentum and energy) . . . . .	23
57	Compute Lagrangian specific volume of the fluid phase . . . . .	25
58	Compute advection term and advance in time . . . . .	26
59	Interpolate from cell to node of the solid phase . . . . .	26
60	Update the particle variables . . . . .	27
61	<b>Numerical examples</b>	27
62	Fluid Flow through isothermal porous media . . . . .	28
63	Isothermal consolidation . . . . .	29
64	Thermal induced cavity flow . . . . .	30
65	Underwater debris flow . . . . .	31
66	Validation of soil response to the seismic loading . . . . .	35
67	Earthquake-induced submarine landslides . . . . .	38

68	<b>Conclusions</b>	43
69	<b>Acknowledgements</b>	44
70	<b>Appendix: Equation derivation</b>	44
71	Evolution of porosity . . . . .	45
72	Momentum conservation . . . . .	45
73	Energy conservation . . . . .	46
74	Advanced Fluid Pressure . . . . .	47
75	Momentum and Energy exchange with an implicit solver . . . . .	48

<sup>76</sup> **Nomenclature**

**General variables**

<u>Variable</u>	<u>Dimensions</u>	<u>Description</u>
$V$	$[L^3]$	Representative volume
$n$		Porosity
$\sigma$	$[ML^{-1}t^{-2}]$	Total stress tensor
$\Delta t$	$[t]$	Time increment
$\mathbf{b}$	$[ML^1t^{-2}]$	Body force
$c_v$	$[L^2t^{-2}T^{-1}]$	Constant volume specific heat
$f_d$	$[MLt^{-2}]$	Drag forces in momentum exchange term
$f^{int}$	$[MLt^{-2}]$	Internal forces
$f^{ext}$	$[MLt^{-2}]$	External forces
$q_{fs}$	$[MLt^{-2}]$	Heat exchange term
$S$		Weighting function
$\nabla S$		Gradient of weighting function

<sup>77</sup>

**Solid phase**

<u>Variable</u>	<u>Dimensions</u>	<u>Description</u>
$m_s$	$[M]$	Solid mass
$\rho_s$	$[ML^{-3}]$	Solid density
$\phi_s$		Solid volume fraction
$\bar{\rho}_s$	$[ML^{-3}]$	Bulk Solid density
$\mathbf{x}_s$	$[L]$	Solid Position vector
$\mathbf{U}_s$	$[Lt^{-1}]$	Solid Velocity vector
$\mathbf{a}_s$	$[Lt^{-2}]$	Solid Acceleration vector
$\sigma'$	$[ML^{-1}t^{-2}]$	Effective Stress tensor
$\epsilon$		Strain tensor
$e_s$	$[L^2t^{-2}]$	Solid Internal energy per unit mass
$T_s$	$[T]$	Solid Temperature
$\mathbf{F}_s$		Solid Deformation gradient
$V_s$	$[L^3]$	Solid Volume

**Fluid phase**

<u>Variable</u>	<u>Dimensions</u>	<u>Description</u>
$m_f$	[M]	Fluid mass
$\rho_f$	[ML <sup>-3</sup> ]	Fluid density
$\phi_f$		Fluid volume fraction
$\bar{\rho}_f$	[ML <sup>-3</sup> ]	Bulk Fluid density
$\mathbf{U}_f$	[Lt <sup>-1</sup> ]	Fluid Velocity vector
$\boldsymbol{\sigma}_f$	[ML <sup>-1</sup> t <sup>-2</sup> ]	Fluid stress tensor
$p_f$	[ML <sup>-1</sup> t <sup>-2</sup> ]	Fluid isotropic pressure
$\boldsymbol{\tau}_f$	[ML <sup>-1</sup> t <sup>-2</sup> ]	Fluid shear stress tensor
$e_f$	[L <sup>2</sup> t <sup>-2</sup> ]	Fluid Internal energy per unit mass
$T_f$	[T]	Fluid Temperature
$v_f$	[L <sup>3</sup> /M]	Fluid Specific volume $\frac{1}{\rho_f}$
$\alpha_f$	[1/T]	Thermal expansion
$\mu$	[ML <sup>-1</sup> t <sup>-1</sup> ]	Fluid viscosity
$V_f$	[L <sup>3</sup> ]	Fluid Volume

**Superscript**

<u>Variable</u>	<u>Dimensions</u>	<u>Description</u>
$n$		Current time step
$L$		Lagrangian values
$n + 1$		Next time step

**Subscript**

$c$	Cell-centered quantity
$p$	Particle quantity
$i$	Node quantity
$FC$	Face-centered Cell face quantity
$L, R$	Left and Right cell faces

79 **Introduction**

80 Many geological natural processes and their interactions with man-made  
81 structures are influenced by soil-fluid-structure interactions. The prediction  
82 of these processes requires a tool that can capture complex interactions  
83 between soil, fluid, and structure, such as the process of submarine land-  
84 slides. Indeed, The offshore infrastructure as well as coastal communities  
85 may be vulnerable to submarine landslides. Submarine landslides contain  
86 three stages: triggering, failure, and post-failure. Erosion or earthquakes can  
87 trigger slope failures in the first stage. Following the failure, sediments move  
88 quickly after the post-failure stage. In other words, solid-like sediments will  
89 behave like a fluid after failure. This phase transition makes the simulation  
90 of submarine landslides a challenging task.

91

92 Due to this phase transition, submarine landslide can be modeled by ei-  
93 ther the Computational Fluid Dynamics (CFD) or the particle-based meth-  
94 ods. For simulating submarine slides, CFD methods solve governing equa-  
95 tions in a full-Eulerian framework [1, 2, 3, 4] with interface capturing tech-  
96 niques. While CFD can handle complex flows (such as turbulent flows), it  
97 cannot account for the triggering mechanism of submarine landslides because  
98 it is not ~~straightforward~~ straightforward to consider 'soil constitutive laws' of  
99 sediment materials in the Eulerian framework. In contrast, particle-based  
100 methods can overcome this problem by using the Lagrangian framework.  
101 These methods have been extensively used to simulate landslides, like Mate-  
102 rial Point Method (MPM) [5], Smooth Particle Hydro Dynamics [6], Particle  
103 Finite Element Method [7], or Coupled Eulerian Lagrangian Method [8]. For  
104 simplicity, these simulations adopt total stress analysis which neglects the  
105 pore pressure development which is key factor triggering slope failures.

106

107 Recent developments in particle-based methods model the coupling of  
108 fluid flows in porous media by sets of Lagrangian particles. For the MPM  
109 family, it is the double-point MPM ([9, 10, 11]) where fluid particles and  
110 solid particles are overlapped in a single computational grid. Even if fluid  
111 flows are considered, particle-based methods have numerical instability in  
112 modeling the fluid flow, which requires additional numerical treatments such  
113 as the B-bar method [9], null-space filter [12], or least square approximation  
114 [13, 14]. Indeed, CFD is a more optimal option for complex fluid flows  
115 especially dealing with large distortions of continuum fluid media. Therefore,

116 it could be ideal to combine the CFD with particle-based methods. More than  
 117 50 particle-based methods have been developed to solve large deformations  
 118 of solids over the last two decades [15], but the MPM appears to be the  
 119 best candidate for coupling with the CFD. Because MPM incorporates a  
 120 stationary mesh during computation, just like CFD. As such, both MPM  
 121 and CFD can be coupled naturally in a unified computational mesh.



*Figure 1: Interaction between soil-fluid-structure*

122

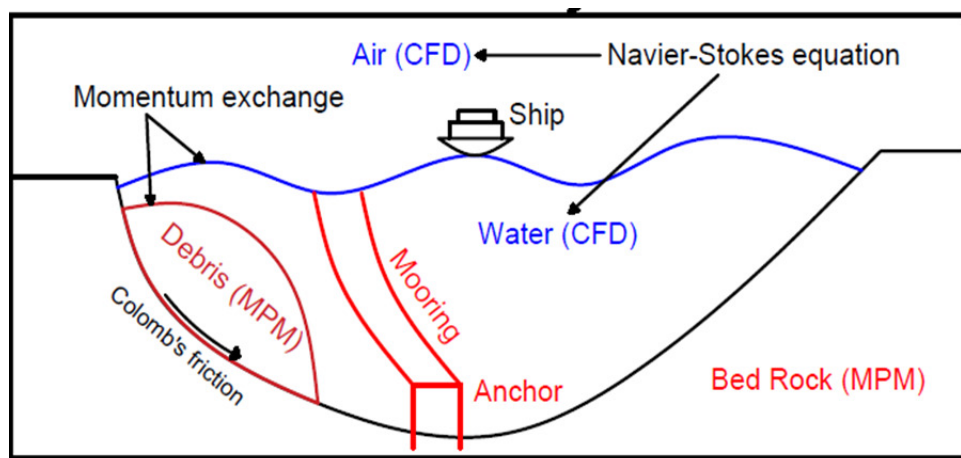


*Figure 2: Coupling of soil-water-structure interaction using MPMICE*

123 A numerical method for simulating soil-fluid-structure interaction (Figure  
124 1) involving large deformations, is presented in this work in order to simu-  
125 late the interaction between sediment (soil), seawater (fluid) and offshore  
126 structures (structure) namely MPMICE (Figure 2). In the MPMICE, the  
127 Material Point Method (MPM) is coupled with the Implicit Continuous Eu-  
128 lerian (ICE). The MPM method is a particle method that allows the porous  
129 soil to undergo arbitrary distortions. The ICE method, on the other hand,  
130 is a conservative finite volume technique with all state variables located at  
131 the cell center (temperature, velocity, mass, pressure). An initial technical  
132 report [16] at Los Alamos National Laboratory provided the theoretical and  
133 algorithmic foundation for the MPMICE, followed by the MPMICE devel-  
134 opment and implementation in the high-performance Uintah computational  
135 framework for simulating fluid-structure interactions [17]. This paper pri-  
136 marily contributes ~~further~~ further to the development of the MPMICE for  
137 analyzing the **soil**-fluid-structure interaction, since sediment should be con-  
138 sidered as a porous media (soil) and not as a solid to capture the evolution  
139 of the pore water pressure. Baumgarten et al. [18] made the first attempt  
140 at coupling the Finite Volume Method with the MPM for the simulation of  
141 soil-fluid interaction. In contrast to the mentioned work, we use implicit time  
142 integration for the multi phase flows instead of explicit time integration for  
143 the single-phase flow.

## 144 **Theory and formulation**

145 This section lay out the theoretical framework for the MPMICE model.  
146 We use the common notation of the continuum ~~meehaniees~~ mechanics with  
147 vector and tensor denoted simply by using bold font and scalar denoted by  
148 using normal font. The notation are shown in Nomenclature.

### 149 *Assumptions*

150 The following assumptions are made for the MPMICE model.

- 151 1. Solid phases (MPM) are described in a Lagrangian formulation while  
152 fluid phases (ICE) are described in an Eulerian formulation in the  
153 framework of continuum mechanics and mixture theory.
- 154 2. Solid grains are incompressible while the fluid phases are compressible.  
155 Solid's thermal expansion is negligible.
- 156 3. There is no mass exchange between solid and fluid phases.
- 157 4. Terzaghi's effective stress is valid.

158 *Governing equations*

159 A representative element volume  $\Omega$  is decomposed by two domains: solid  
160 domains  $\Omega_s$  and fluid domains  $\Omega_f$ . Then, all domains are homogenized  
161 into two overlapping continua. Considering the volume fraction of solid  
162  $\phi_s = \Omega_s/\Omega$  and fluid  $\phi_f = \Omega_f/\Omega$  with the true (or Eulerian) porosity  
163  $n = \sum \phi_f$  of the representative element volume, the average density of solid  
164 and fluid phases are defined as:

165

$$\bar{\rho}_s = \phi_s \rho_s, \quad \bar{\rho}_f = \phi_f \rho_f \quad (1)$$

166 The mass of solid and fluid phases are:

167

$$m_s = \int_{\Omega_s} \rho_s dV = \bar{\rho}_s V, \quad m_f = \int_{\Omega_f} \rho_f dV = \bar{\rho}_f V \quad (2)$$

168 Reviewing the Terzaghi's effective stress concept for the saturated porous  
169 media, the total stress  $\boldsymbol{\sigma}$  is calculated by:

170

$$\boldsymbol{\sigma} = \boldsymbol{\sigma}' - p_f \mathbf{I} \quad (3)$$

171 The balance equations are derived based on the mixture theory. The rep-  
172 resentative thermodynamic state of the fluid phases are given by the vector  
173  $[m_f, \mathbf{U}_f, e_f, T_f, v_f]$  which are mass, velocity, internal energy, temperature,  
174 specific volume. The representative state of the solid phases are given by the  
175 vector  $[m_s, \mathbf{U}_s, e_s, T_s, \boldsymbol{\sigma}', p_f]$  which are mass, velocity, internal energy, temper-  
176 ature, effective stress and pore water pressure. The derivation is presented  
177 in detail in the Appendix.

178

---

179 Mass Conservation

180 The mass balance equations for both fluid (e.g., water, air) and solid phases  
181 are:

182

$$\frac{1}{V} \frac{\partial m_f}{\partial t} + \nabla \cdot (m_f \mathbf{U}_f) = 0, \quad \frac{1}{V} \frac{D_s m_s}{Dt} = 0 \quad (4)$$

183 Solving the mass balance equation leads to:

$$\frac{D_s n}{Dt} = \phi_s \nabla \cdot \mathbf{U}_s \quad (5)$$

184

---

185 Momentum Conservation

<sup>186</sup> The momentum balance ~~equation-equations~~ for the fluid phases (e.g., water,  
<sup>187</sup> air) are:

$$\frac{1}{V} \left[ \frac{\partial(m_f \mathbf{U}_f)}{\partial t} + \nabla \cdot (m_f \mathbf{U}_f \mathbf{U}_f) \right] = -\phi_f \nabla p_f + \nabla \cdot \boldsymbol{\tau}_f + \bar{\rho}_f \mathbf{b} + \sum \mathbf{f}_d \quad (6)$$

<sup>188</sup> The momentum balance ~~equation-equations~~ for the solid phases are:

$$\frac{1}{V} \frac{D_s(m_s \mathbf{U}_s)}{Dt} = \nabla \cdot (\boldsymbol{\sigma}') - \phi_s \nabla p_f + \bar{\rho}_s \mathbf{b} + \sum \mathbf{f}_{fric} - \sum \mathbf{f}_d \quad (7)$$

---

#### 189 Energy Conservation

<sup>190</sup> The internal energy balance ~~equation-equations~~ for the fluid phases (e.g.,  
<sup>191</sup> water, air) are:

$$\frac{1}{V} \left[ \frac{\partial(m_f e_f)}{\partial t} + \nabla \cdot (m_f e_f \mathbf{U}_f) \right] = -\bar{\rho}_f p_f \frac{D_f v_f}{Dt} + \boldsymbol{\tau}_f : \nabla \mathbf{U}_f + \nabla \cdot \mathbf{q}_f + \sum q_{sf} \quad (8)$$

<sup>192</sup> The internal energy balance ~~equation-equations~~ for the solid phase ~~is~~are:

$$\frac{m_s}{V} c_v \frac{D_s(T_s)}{Dt} = \boldsymbol{\sigma}' : \frac{D_s(\boldsymbol{\epsilon}_s^p)}{Dt} + \nabla \cdot \mathbf{q}_s - \sum q_{sf} \quad (9)$$

<sup>193</sup> where  $c_v$  is the specific heat at constant volume of the solid materials.

---

<sup>194</sup> Closing the systems of equations, the following additional models are needed:

<sup>195</sup> (1) A constitutive equation to describe the stress - strain behaviour of solid  
<sup>196</sup> phase (computing effective stress  $\boldsymbol{\sigma}'$ ).  
<sup>197</sup> (2) Optional turbulent model to compute the viscous shear stress  $\boldsymbol{\tau}_f$ .  
<sup>198</sup> (3) Frictional forces  $\mathbf{f}_{fric}$  for the contact for soil-structure interaction be-

<sup>199</sup> tween solid/porous materials with the friction coefficient  $\mu_{fric}$ .  
<sup>200</sup> (4) Exchange momentum models (computing drag force  $\mathbf{f}_d$ ) for interaction  
<sup>201</sup> between materials.

<sup>202</sup> (5) Energy exchange models (computing temperature exchange term  $q_{sf}$ ) for  
<sup>203</sup> interaction between materials.  
<sup>204</sup> (6) An equation of state to establish relations between thermodynamics vari-

<sup>205</sup> ables of each fluid materials  $[P_f, \bar{\rho}_f, v_f, T_f, e_f]$ .

208 Four thermodynamic relations for the equation of states are:

$$\begin{aligned} e_f &= e_f(T_f, v_f) \\ P_f &= P_f(T_f, v_f) \\ \phi_f &= v_f \bar{\rho}_f \\ 0 &= n - \sum_{f=1}^{N_f} v_f \bar{\rho}_f \end{aligned} \quad (10)$$

209 *Constitutive soil model*

210 As a result of the explicit MPM formulation, we can derive the consti-  
 211 tutive law in the updated Lagrangian framework of "small strain - large  
 212 deformation". Therefore, the rotation of the particles (representative ele-  
 213 ment volume) is manipulated by rotating the Cauchy stress tensor. First,  
 214 the deformation gradient is decomposed into the polar rotation tensor  $\mathbf{R}_s^{n+1}$   
 215 and ~~sketch~~-stretch tensor  $\mathbf{V}_s^{n+1}$  as:

$$\mathbf{F}_s^{n+1} = \mathbf{V}_s^{n+1} \mathbf{R}_s^{n+1} \quad (11)$$

216 Then, before calling the constitutive model, the stress and strain rate tensor  
 217 are rotated to the reference configuration as:

$$\boldsymbol{\sigma}'^{n*} = (\mathbf{R}_s^{n+1})^T \boldsymbol{\sigma}'^{n*} \mathbf{R}_s^{n+1} \quad (12)$$

$$\delta\boldsymbol{\epsilon}^{n*} = (\mathbf{R}_s^{n+1})^T \delta\boldsymbol{\epsilon}_s^{n*} \mathbf{R}_s^{n+1} \quad (13)$$

219 Using the constitutive model with the input tensors  $\boldsymbol{\sigma}'^{n*}, \delta\boldsymbol{\epsilon}^{n*}$  to compute  
 220 the Cauchy stress tensor at the advanced time step  $\boldsymbol{\sigma}'^{n+1*}$  then rotating it  
 221 back to current configuration as:

$$\boldsymbol{\sigma}'^{n+1} = \mathbf{R}_s^{n+1} \boldsymbol{\sigma}'^{n+1*} (\mathbf{R}_s^{n+1})^T \quad (14)$$

222 In this paper, we adopt the hyper-elastic Neo Hookean model for the structure  
 223 materials and additionally Mohr-Coulomb failure criteria for the soil (porous  
 224 media) materials. The Cauchy stress of the hyper-elastic Neo Hookean model  
 225 can be written as:

$$\boldsymbol{\sigma}' = \frac{\lambda \ln(J)}{J} + \frac{\mu}{J} (\mathbf{F} \mathbf{F}^T - \mathbf{J}) \quad (15)$$

226 where  $\lambda$  and  $\mu$  are bulk and shear modulus ad  $J$  is the determinant of the  
 227 deformation gradient  $\mathbf{F}$ . And the yield function  $f$  and flow potentials  $g$  of

<sup>228</sup> the Mohr-Coulomb can be written as:

$$\begin{aligned} f &= \sigma'_1 - \sigma'_3 - 2c' \cos(\phi') - (\sigma'_1 + \sigma'_3) \sin(\phi') \\ g &= \sigma'_1 - \sigma'_3 - 2c' \cos(\psi') - (\sigma'_1 + \sigma'_3) \sin(\psi') \end{aligned} \quad (16)$$

<sup>229</sup> where the  $c'$ ,  $\phi'$  and  $\psi'$  are cohesion and friction angle and dilation angle.  $\sigma'_1$   
<sup>230</sup> and  $\sigma'_3$  are maximum and minimum principal stress.

<sup>231</sup> *Turbulent model*

<sup>232</sup> The turbulent effect is modelled using a statistical approach namely large-  
<sup>233</sup> eddy simulation. In this approach, the micro-scale turbulent influence in the  
<sup>234</sup> dynamics of the macro-scale motion is computed through simple models like  
<sup>235</sup> Smagorinsky model. In the Smagorinsky ~~mode~~model, the residual stress  
<sup>236</sup> tensor is:

$$\tau_{ij} = 2\mu_{eff}(\bar{S}_{ij} - \frac{1}{3}\delta_{ij}\bar{S}_{kk}) + \frac{1}{3}\delta_{ij}\tau_{kk} \quad (17)$$

<sup>237</sup> where the strain rate tensor is given by:..

$$\bar{S}_{ij} = \frac{1}{2}(\frac{\delta \bar{U}_i}{\delta x_j} + \frac{\delta \bar{U}_j}{\delta x_i}) \quad (18)$$

<sup>238</sup> and the effective viscosity is sum of molecular viscosity and turbulent vis-  
<sup>239</sup> cosity  $\mu_{eff} = \mu + \mu_t$  in which the turbulent viscosity  $\mu_t$  is calculated by:..

$$\mu_t = (C_s \Delta)^2 \sqrt{2\bar{S}_{ij}\bar{S}_{ij}} \quad (19)$$

<sup>241</sup> where  $C_s$  is the Smagorinsky constant with the value of 0.1 and  $\Delta = \sqrt[3]{dxdydz}$   
<sup>242</sup> is the grid size that defines the subgrid length scale.

<sup>243</sup> *Frictional force for soil-structure interaction*

<sup>244</sup> MPMICE includes a contactlaw-contact law for the interaction between  
<sup>245</sup> soil and structure using the first Coulomb friction contact for MPM presented  
<sup>246</sup> by Bardenhagen et al. ([19]). The magnitude of the friction force at the  
<sup>247</sup> contact depends on the friction coefficient  $\mu_{fric}$  and the normal force  $\mathbf{f}_{norm}$   
<sup>248</sup> computed from the projection of the contact force in the normal direction.

$$\mathbf{f}_{fric} = \mu_{fric} \mathbf{f}_{norm} \quad (20)$$

<sup>249</sup> The contact determines whether the soil is sliding or sticking to the structure  
<sup>250</sup> by comparing the friction force with the sticking force  $\mathbf{f}_{stick}$  computed from

251 the projection of the contact force in the tangent direction as:

$$\begin{aligned} & \text{if } \mathbf{f}_{fric} \geq \mathbf{f}_{stick} \text{ no sliding} \\ & \text{if } \mathbf{f}_{fric} < \mathbf{f}_{stick} \text{ sliding occurs} \end{aligned} \quad (21)$$

252 Frictional sliding between solid materials also generates dissipation and the  
253 work rate generated from the sliding can be calculated as:

$$\Delta W_{friction} = \mathbf{f}_{fric} d \quad (22)$$

254 where  $d$  is the sliding distance which can be computed based on the sliding  
255 velocity between two materials.

256 *Momentum and Energy exchange model*

257 Currently, the energy exchange coefficient  $H_{sf}$  is assumed to be constant  
258 for the sake of simplicity. Then the energy exchange can be written as:

$$q_{sf} = H_{sf}(T_f - T_s) \quad (23)$$

259 On the other hand, the drag force can be calculated as:

$$f_d = K(\mathbf{U}_s - \mathbf{U}_f) \quad (24)$$

260 For the momentum exchange between fluid flows and porous media, we as-  
261 sume that the drag force  $\mathbf{f}_d$  depends on the average grain size of the grains  $D_p$ ,  
262 the porosity  $n$ , the fluid viscosity  $\mu_f$ , and is proportional to the relative velocities of soil grains and fluid  $(\mathbf{U}_s - \mathbf{U}_f)$ . Based on recent  
263 investigation of CFD simulations of fluid flow around mono- and bi-disperse  
264 packing of spheres for  $0.1 < \phi_s < 0.6$  and  $Re < 1000$  [20]. The drag force is  
265 given by:

267

$$\mathbf{f}_d = \frac{18\phi_s(1-\phi_s)\mu_f}{D_p^2} F(\phi_s, Re)(\mathbf{U}_s - \mathbf{U}_f) \quad (25)$$

268 where Reynolds number  $Re$  are computed as:

$$Re = \frac{n\rho_f D_p}{\mu_f} \|(\mathbf{U}_s - \mathbf{U}_f)\| \quad (26)$$

269 The function  $F(\phi_s, Re)$  can be calculated as:

$$F(\phi_s, Re) = F(\phi_s, 0) + \frac{0.413Re}{24(1-\phi_s)^2} \left( \frac{(1-\phi_s)^{-1} + 3\phi_s(1-\phi_s) + 8.4Re^{-0.343}}{1 + 10^{3\phi_s} Re^{-(1+4\phi_s)/2}} \right) \quad (27)$$

270 where the low Reynold coefficient  $F(\phi_s, Re \rightarrow 0)$  is:

$$F(\phi_s, 0) = \frac{10\phi_s}{(1 - \phi_s)^2} + (1 - \phi_s)^2(1 + 1.5\sqrt{\phi_s}) \quad (28)$$

271 When validating the model with analytical solution, it requires to know the  
 272 hydraulic conductivity  $\underline{K}$ . In such case, we convert the equation (29) to  
 273 Kozeny-Carman formula by assuming  $F(\phi_s, Re) = 10\phi_s/(1 - \phi_s)^2$ , ~~then the~~  
 274 ~~leading to~~

$$\underline{f_d} = \frac{180\phi_s^2\mu_f}{D_p^2(1 - \phi_s)} (\underline{U_s} - \underline{U_f}) \quad (29)$$

275 ~~equation Then, the draging force following the Darcy law is given by:~~

$$\underline{f_d} = \frac{n^2\mu_f}{\kappa} (\underline{U_s} - \underline{U_f}) \quad (30)$$

276 ~~equation where  $\kappa$  being intrinsic permeability of soil which can be written~~  
 277 ~~as:~~

$$\kappa = \frac{K\mu_f}{\rho_f g} \quad (31)$$

278 ~~equation As such, the~~ hydraulic conductivity will be expressed as  $D_p^2(1 - \phi_s)^3 / 180\mu_f\phi_s^2$ .  
 279 ~~∴~~

$$K = \frac{D_p^2(1 - \phi_s)^3}{180\phi_s^2\mu_f} \rho_f g \quad (32)$$

280 ~~equation~~

281 *Solving momentum and energy exchange with an implicit solver*

282 The derivation of the implicit integration for the momentum exchange is  
 283 presented in the Appendix's section 'Momentum and energy exchange with  
 284 an implicit solver'. The linear equations for multi phases i,j=1:N has the  
 285 form ~~as:~~

$$\begin{vmatrix} (1 + \beta_{ij}) & -\beta_{ij} \\ -\beta_{ji} & (1 + \beta_{ji}) \end{vmatrix} \begin{vmatrix} \Delta \mathbf{U}_i \\ \Delta \mathbf{U}_j \end{vmatrix} = \begin{vmatrix} \beta_{ij}(\mathbf{U}_i^* - \mathbf{U}_j^*) \\ \beta_{ji}(\mathbf{U}_i^* - \mathbf{U}_j^*) \end{vmatrix}$$

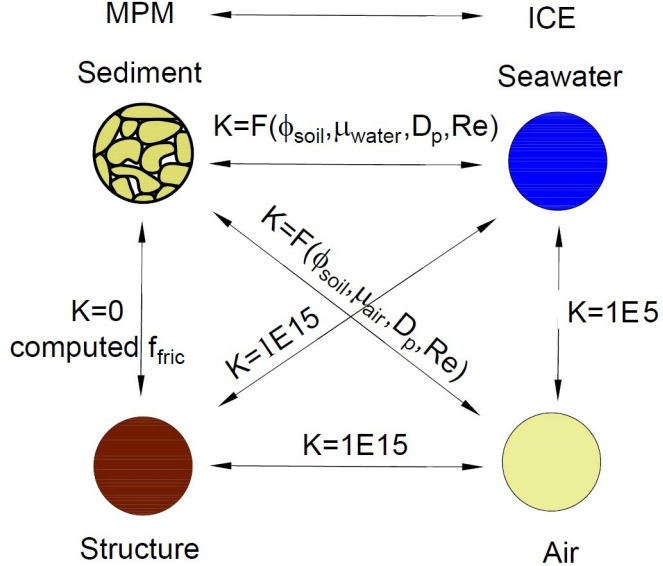


Figure 3: Momentum exchange coefficient between materials

286 where the intermediate velocity for fluid phases  $f=1:N_f$  and for solid/porous  
 287 phases  $s=1:N_s$  can be calculated by:

$$\begin{aligned} \mathbf{U}_f^* &= \mathbf{U}_f^n + \Delta t \left( -\frac{\nabla P_f^{n+1}}{\rho_f^n} + \frac{\nabla \cdot \boldsymbol{\tau}_f^n}{\bar{\rho}_f^n} + \mathbf{b} \right) \\ \mathbf{U}_s^* &= \mathbf{U}_s^n + \Delta t \left( \frac{\nabla \cdot \boldsymbol{\sigma}'^n}{\bar{\rho}_s^n} - \frac{\nabla P_f^{n+1}}{\rho_s} + \mathbf{b} \right) \end{aligned} \quad (33)$$

288 Also, the momentum exchange coefficient can be computed at every time  
 289 step as  $\beta_{12} = K/\bar{\rho}_f^n$  and  $\beta_{21} = K/\bar{\rho}_s^n$  with the coefficient depending on the  
 290 different type of interactions (see Figure 3) as for example:

291

- 292 1. The drag force is set to zero in soil-structure interactions, and instead  
 293 the frictional force is computed.
- 294 2. As a result of fluid-structure interaction, the momentum exchange coef-  
 295 ficient should be extremely high (1E15) when the solid material points  
 296 are considered to be zero-porosity/zero-permeability.
- 297 3. In the case of soil-fluid interaction, the drag force is calculated using  
 298 the equation (29). Considering that air has a much lower viscosity than

299 water, its drag force is much lower than the drag force of water in a  
 300 pore.

301 4. A momentum exchange coefficient of 1E5 is applied between multiphase  
 302 flows. This value is far higher than reality [21], but it is necessary to  
 303 have enough numerical stability to conduct simulations in the numerical  
 304 example.

305 Similar approach applied for the energy exchange term leading to:

$$\begin{vmatrix} (1 + \eta_{ij}) & -\eta_{ij} \\ -\eta_{ji} & (1 + \eta_{ji}) \end{vmatrix} \frac{|\Delta T_i|}{|\Delta T_j|} = \frac{|\eta_{ij}(T_i^n - T_j^n)|}{|\eta_{ji}(T_j^n - T_i^n)|}$$

306 with  $\eta$  ~~is being~~ the energy exchange coefficient.

307 *Equation of state for fluid phases*

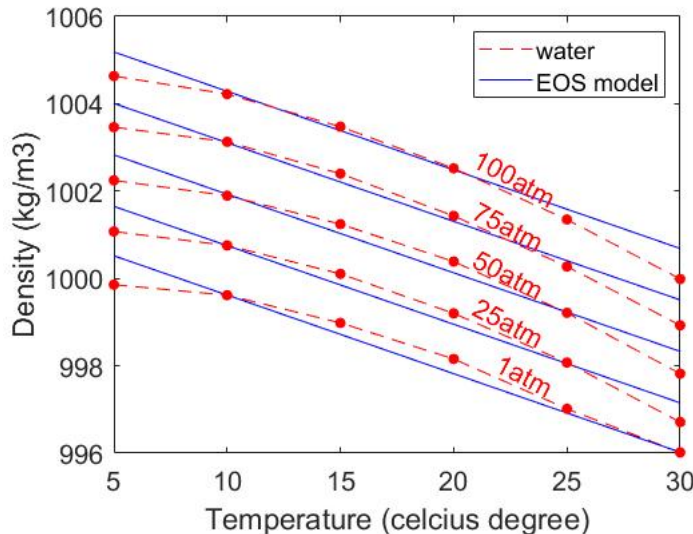


Figure 4: Equation of state of water

308 The equation of state establishes relations between thermodynamics vari-  
 309 ables  $[P_f, \rho_f, T_f]$ . The choice of the equation of state depends on the types  
 310 of the fluid materials. For example, for the air, it is possible to assume the  
 311 equation of state for the perfect gas which obeys:

$$P_f = \rho_f R T_f \quad (34)$$

312 where  $R$  is the gas constant. For the water, a simple linear equation of state  
 313 is in the following form:

$$P_f = P_{ref} + K_f(\rho_f - \rho_{ref} - \alpha_f(T_f - T_{ref})) \quad (35)$$

314 where reference pressure  $P_{ref} = 1$  atm = 101325 Pa, reference temperature  
 315  $T_{ref} = 10^\circ\text{C}$ , reference density  $\rho_{ref} = 999.8 \text{ kg/m}^3$ , the bulk modulus of water  
 316  $K_f = 2 \text{ GPa}$ , and the water thermal expansion  $\alpha_f = 0.18 \text{ }^\circ\text{C}^{-1}$ . Equation  
 317 (35) matches well with the state of the water (see Figure 4).

318 **Numerical implementation**

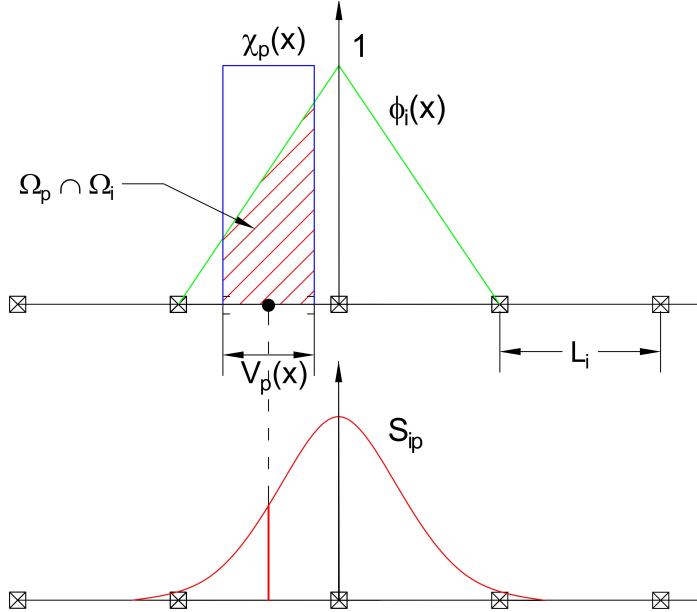


Figure 5: GIMP weighting function (red as a convolution of the linear basis shape function (green) and the charateristic-charateristic function (blue))

319 The fluid phases are discretized in the grid with the state variables stored  
 320 at the centroid of the cells  $[\rho_{fc}, \mathbf{U}_{fc}, T_{fc}, v_{fc}]$  while the  
 321 solid phase is discretized in the particles with the state variables  $[m_{sp}, \mathbf{U}_{sp}, T_{sp}, \boldsymbol{\sigma}'_{sp}]$ .  
 322 In the Material Point Method, we use the generalized interpolation technique  
 323 [22] using the weight function as a convolution of a grid shape function  $N_i(\mathbf{x})$

324 in a nodal domain  $\Omega_i$  and a characteristic function  $\chi_p(\mathbf{x})$  in a particle domain  
 325  $\Omega_p$  with the volume  $V_p(\mathbf{x})$  as follows:

$$S_{ip} = \frac{1}{V_p} \int_{\Omega_i \cap \Omega_p} N_i(\mathbf{x}) \chi_p(\mathbf{x}) d\mathbf{x} \quad (36)$$

326 where the volume  $V_p(\mathbf{x})$  of the material point p can be calculated as:

$$V_p = \int_{\Omega_p} \chi_p(\mathbf{x}) d\mathbf{x} \quad (37)$$

327 The ~~charateristic~~ characteristic function is the Heaviside function as  $\chi_p =$   
 328 1 if  $\mathbf{x} \in \Omega_p$ , otherwise 0 (see Figure 5). For the interpolation of the centroid  
 329 of the cell, the linear basis function is used as:

$$S_{ci} = N_i(\mathbf{x}_c) \quad (38)$$

330 The time discretization are solved using the following steps:~~-~~ sidewaysfigure

### 331 *Interpolation from Solid Particle to Grid*

332 The nodal values of the solid state (mass, velocity, temperature, volume)  
 333 are:

$$\begin{aligned} m_{si}^n &= \sum S_{ip} m_{sp} \\ \mathbf{U}_{si}^n &= \frac{\sum S_{ip} (m\mathbf{U})_{sp}^n}{m_{si}^n} \\ T_{si}^n &= \frac{\sum S_{ip} (mT)_{sp}^n}{m_{si}^n} \\ V_{si}^n &= \frac{\sum S_{ip} (mV)_{sp}^n}{m_{si}^n} \\ \boldsymbol{\sigma}_{si}^n &= \frac{\sum S_{ip} (\boldsymbol{\sigma}V)_{sp}^n}{V_{si}^n} \end{aligned} \quad (39)$$

334 The nodal internal forces is calculated by:~~-~~

$$\mathbf{f}_{si}^{int,n} = - \sum \nabla S_{ip} (\boldsymbol{\sigma}'_{sp})^n V_{sp}^n \quad (40)$$

335 The nodal external forces  $f_{si}^{ext,n}$  and ~~extra momentum from contact forces~~  
 336 the nodal frictional forces  $f_{si}^{fric}$  from contact between materials are com-  
 337 puted here. ~~The nodal velocity and nodal temperature are applied boundary~~

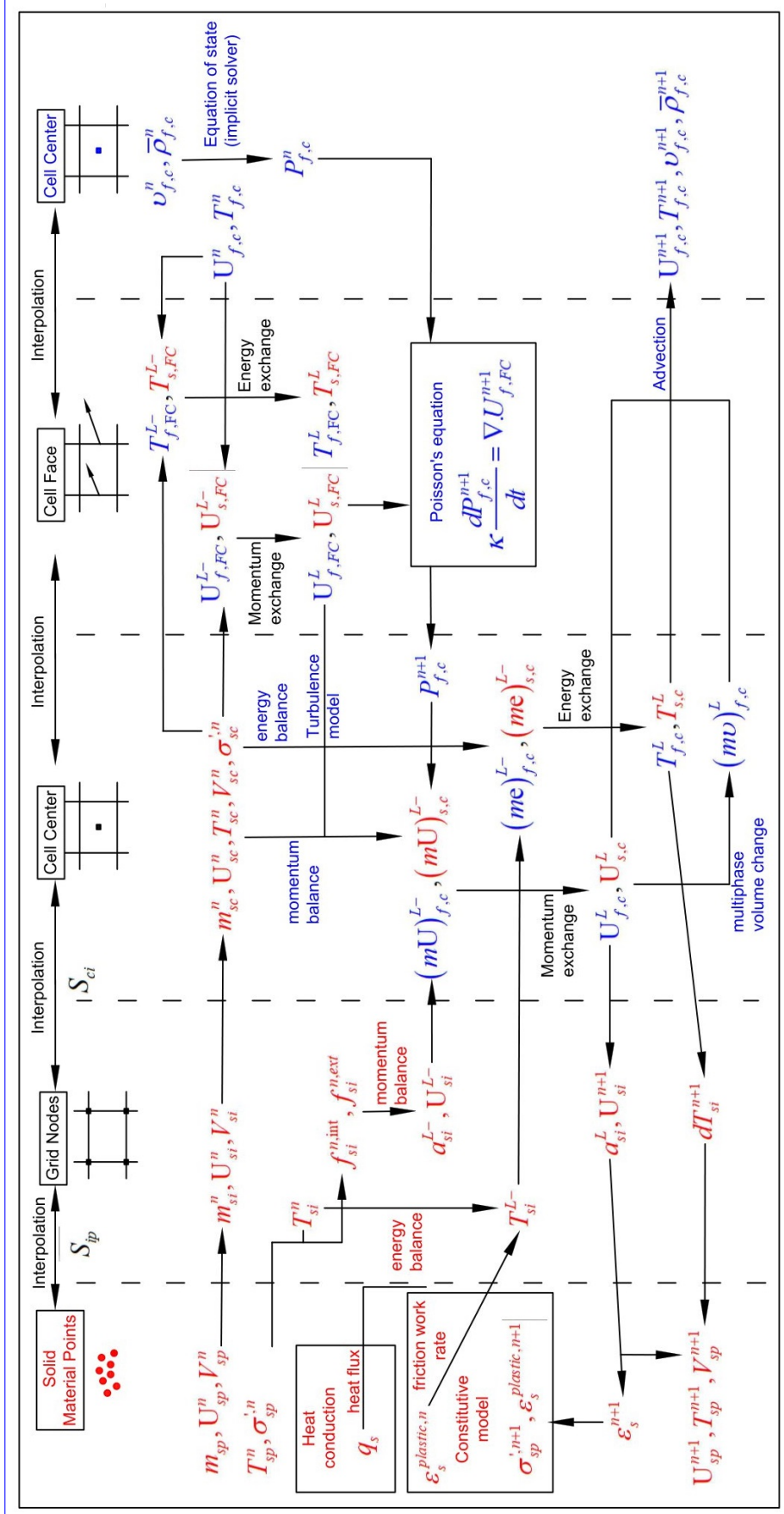


Figure 6: Numerical implementation of MPMCE

338 **conditions.**

339 Then we compute the solid cell variables as:

$$\begin{aligned} m_{sc}^n &= \sum S_{ci} m_{si} \\ \rho_{sc}^n &= \frac{m_{sc}^n}{V} \\ \mathbf{U}_{sc}^n &= \sum S_{ci} \mathbf{U}_{si}^n \\ T_{sc}^n &= \sum S_{ci} T_{si}^n \\ V_{sc}^n &= \sum S_{ci} V_{si}^n \\ \boldsymbol{\sigma}_{sc}^n &= \sum S_{ci} \boldsymbol{\sigma}_{si}^n \end{aligned} \tag{41}$$

340 *Compute equation of state for fluid phase*

341 Considering the total fluid material The total fluid material volume of a  
342 cell is:

$$V_{total} = \sum_{f=1}^{N_f} M_f v_f \tag{42}$$

343 Then we We need to find  $P_{eq}$   $P_{f,e}$  which allows each fluid materials obey their  
344 equation of states  $[P_f, \rho_f, v_f, T_f, e_f]$  but also allow mass of all fluid materials  
345 to fill the entire the pore volume without ongoing compression or expansion  
346 following the condition as follows:

$$0 = n - \sum_{f=1}^{N_f} v_f \bar{\rho}_f \tag{43}$$

347 Then, we can use he the Newton-Raphson interation to find the value of  $P_{eq}$   
348  $P_{f,e}$  which satisfies the equation (42, 43) and each equation of states of each  
349 fluid materials.

350 Compute faced-centered velocity Compute cell face velocity

351 Following the derivation in the Appendix: Advanced Fluid Pressure, we  
352 first compute the fluid face-centered velocity as cell face velocity as:

$$\mathbf{U}_{f,FC}^{*L} = \frac{(\bar{\rho} \mathbf{U})_{f,FC}^n}{\bar{\rho}_{f,FC}^n} + \Delta t \left( -\frac{\nabla^{FC} P_{eq}}{\rho_{f,FC}^n} \frac{\nabla^{FC} P_{f,c}^n}{\rho_{f,FC}^n} + \frac{\nabla^{FC} \cdot \boldsymbol{\tau}^n}{\bar{\rho}_{s,FC}} + \mathbf{b} \right) \tag{44}$$

353 The equation (44) is discretized in three dimension (noted that  $\nabla^{FC} \cdot \boldsymbol{\tau} = 0$ ),  
 354 for example the discretized equation in the x direction is:

$$U_{fx}^{L-} = \frac{(\bar{\rho}U)_{fx,R}^n + (\bar{\rho}U)_{fx,L}^n}{\bar{\rho}_{fx,L}^n + \bar{\rho}_{fx,R}^n} + \Delta t \left( -\frac{2(v_{fx,L}^n v_{fx,R}^n)}{v_{fx,L}^n + v_{fx,R}^n} \frac{P_{f,cx,R}^n - P_{f,cx,L}^n}{\Delta x} + b_x \right) \quad (45)$$

355 The face-centered cell face solid velocity can be calculated as:

$$\mathbf{U}_{s,FC}^{*\underline{L-}} = \frac{(\bar{\rho}\mathbf{U})_{s,FC}^n}{\bar{\rho}_{s,FC}^n} + \Delta t \left( \frac{\nabla^{FC} \cdot \boldsymbol{\sigma}_c'^n}{\bar{\rho}_{s,FC}^n} - \frac{\nabla^{FC} P_{eq} \nabla^{FC} P_{f,c}^n}{\bar{\rho}_s} + \mathbf{b} \right) \quad (46)$$

356 The equation (46) is discretized in three dimension (noted that  $\nabla^{FC} \cdot \boldsymbol{\sigma}_{ij} = 0$   
 357 with  $i \neq j$ ), for example the discretized equation in the x direction is:

$$U_{sx}^{L-} = \frac{(\bar{\rho}U)_{sx,R}^n + (\bar{\rho}U)_{sx,L}^n}{\bar{\rho}_{sx,L}^n + \bar{\rho}_{sx,R}^n} + \Delta t \left( \frac{2(\sigma_{xx,R} - \sigma_{xx,L})}{(\bar{\rho}_{sx,L}^n + \bar{\rho}_{sx,R}^n) \Delta x} - \frac{P_{f,cx,R}^n - P_{f,cx,L}^n}{\rho_s \Delta x} + b_x \right) \quad (47)$$

358 Computing the modified faced-centered Then, we compute the modified cell  
 359 face velocity  $\mathbf{U}_{FC}^L$  considering the momentum exchange (see the Appendix:  
 360 Momentum exchange with an implicit solve) as follows:

$$\begin{aligned} \mathbf{U}_{f,FC}^L &= \mathbf{U}_{f,FC}^{*\underline{L-}} + \Delta \mathbf{U}_{f,FC} \\ \mathbf{U}_{s,FC}^L &= \mathbf{U}_{s,FC}^{*\underline{L-}} + \Delta \mathbf{U}_{s,FC} \end{aligned} \quad (48)$$

361 Solving the linear equation below is solved to obtain the increment of  
 362 velocity with  $i,j = 1 : N$  as:

$$\begin{vmatrix} (1 + \beta_{ij}) & -\beta_{ij} \\ -\beta_{ji} & (1 + \beta_{ji}) \end{vmatrix} \begin{vmatrix} \Delta \mathbf{U}_{i,FC} \\ \Delta \mathbf{U}_{j,FC} \end{vmatrix} = \begin{vmatrix} \beta_{ij} (\mathbf{U}_{i,FC}^{*\underline{L-}} - \mathbf{U}_{j,FC}^{*\underline{L-}}) \\ \beta_{ji} (\mathbf{U}_{j,FC}^{*\underline{L-}} - \mathbf{U}_{i,FC}^{*\underline{L-}}) \end{vmatrix}$$

363 Compute faced-centered temperature Compute cell face temperature

364 Similar to the velocity, the faced temperature is computed, for example  
 365 in x direction, as:

$$\begin{aligned} \underbrace{T_{fx}^{\underline{nL-}}}_{\text{gathered}} &= \frac{(\bar{\rho}T)_{fx,R}^n + (\bar{\rho}T)_{fx,L}^n}{\bar{\rho}_{fx,L}^n + \bar{\rho}_{fx,R}^n} \\ \underbrace{\frac{T_{fx}}{T_{sx}^{L-}}}_{\text{gathered}} &= \frac{(\bar{\rho}T)_{sx,R}^n + (\bar{\rho}T)_{sx,L}^n}{\bar{\rho}_{sx,L}^n + \bar{\rho}_{sx,R}^n} \end{aligned} \quad (49)$$

366 equation Computing the modified faced-centered Then, we compute the  
 367 modified cell face temperature  $T_{FC}^L$  considering the energy exchange (see  
 368 the Appendix: Momentum and energy exchange with an implicit solver) as  
 369 follows:

$$\begin{aligned} T_{f,FC}^L &= T_{f,FC}^{\text{nL}} + \Delta T_{f,FC} \\ T_{s,FC}^L &= T_{s,FC}^{\text{nL}} + \Delta T_{s,FC} \end{aligned} \quad (50)$$

370 Solving the linear equation below to obtain is solved to determine the  
 371 increment of velocity with  $i,j = 1 : N$  as:

$$\begin{vmatrix} (1 + \eta_{ij}) & -\eta_{ij} \\ -\eta_{ji} & (1 + \eta_{ji}) \end{vmatrix} \begin{vmatrix} \Delta T_{i,FC} \\ \Delta T_{j,FC} \end{vmatrix} = \begin{vmatrix} \eta_{ij}(T_{i,FC}^{\text{nL}} - T_{j,FC}^{\text{nL}}) \\ \eta_{ji}(T_{j,FC}^{\text{nL}} - T_{i,FC}^{\text{nL}}) \end{vmatrix}$$

### 372 Compute fluid pressure (implicit scheme)

373 For single phase flow, the increment of the fluid pressure can be computed  
 374 as:

$$\kappa_f \frac{\Delta P}{dt} = \nabla^c \cdot \mathbf{U}_{f,FC}^{n+1} \quad (51)$$

375 For multi-phase flows, the increment of the fluid pressure of the mixture can  
 376 be computed as:

$$\kappa \frac{\Delta P}{dt} = \sum_{f=1}^{N_f} \nabla^c \cdot (\phi_{f,FC} \mathbf{U}_{f,FC})^{n+1} \quad (52)$$

377 where  $\kappa = \sum_{f=1}^{N_f} (\phi_{f,FC} \kappa_f) / \sum_{f=1}^{N_f} (\phi_{f,FC})$ . Then, the fluid pressure at cell  
 378 center is:

$$P_c^{n+1} = P_c^{\text{eqc}} + \Delta P_c^n \quad (53)$$

379 Finally, the faced-centered cell face advanced fluid pressure is:

$$P_{FC}^{n+1} = \left( \frac{P_{c,L}^{n+1}}{\bar{\rho}_{f,L}^n} + \frac{P_{c,R}^{n+1}}{\bar{\rho}_{f,R}^n} \right) / \left( \frac{1}{\bar{\rho}_{f,L}^n} + \frac{1}{\bar{\rho}_{f,R}^n} \right) = \left( \frac{P_{c,L}^{n+1} \bar{\rho}_{f,R}^n + P_{c,R}^{n+1} \bar{\rho}_{f,L}^n}{\bar{\rho}_{f,L}^n \bar{\rho}_{f,R}^n} \right) \quad (54)$$

### 380 Compute viscous shear stress term of the fluid phase

381 This part compute the viscous shear stress  $\Delta(m\mathbf{U})_{fc,\tau} \Delta(m\mathbf{U})_{f,\text{ext}}$  for a  
 382 single viscous compressible Newtonian fluid and optionally shear stress  
 383 induced by the turbulent model.

384    *Compute nodal internal temperature of the solid phase*

385    The nodal internal temperature rate is computed based on the heat con-  
 386    duction model as below:

$$dT_{si}^{L-} = \frac{(\Delta W_{si}^n + \Delta W_{fric,i}^n + \nabla^i \cdot \mathbf{q}_{si}^n)}{m_{si}^n c_v} \quad (55)$$

387    where  $\Delta W_{si}^n = \boldsymbol{\sigma}' : \frac{D_s(\boldsymbol{\epsilon}_s^p)}{Dt}$  is the mechanical work rate computed from the  
 388    constitutive model with  $\boldsymbol{\epsilon}_s^p$  is the plastic strain,  $\Delta W_{fric,i}^n$  is the work rate  
 389    ~~eompted~~computed from the contact law due to the frictional sliding between  
 390    solid materials. The heat flux is  $\mathbf{q}_s = \bar{\rho}_s \beta_s \nabla T_s$  with  $\beta_s$  being the thermal  
 391    conductivity of the solid materials.

$$T_{si}^{L-} = T_{si}^n + dT_{si}^{L-} \quad (56)$$

392    *Compute and integrate acceleration of the solid phase*

393    After interpolating from material points to the nodes, the nodal acceler-  
 394    ~~ation and velocity are ealculate bycalculated by:~~

$$\mathbf{a}_{si}^{L-} = \frac{\mathbf{f}_{si}^{int,n} + \mathbf{f}_{si}^{ext,n}}{m_{si}^n} + \mathbf{g} \quad (57)$$

$$\mathbf{U}_{si}^{L-} = \mathbf{U}_{si}^n + \mathbf{a}_{si}^{L-} \Delta t \quad (58)$$

396    *Compute Lagrangian value (mass, momentum and energy)*

397    For the fluid phase, the linear momentum rate, the energy rate are:~

$$\Delta(m\mathbf{U})_{fc} = V n_c^n \nabla^c P_c^{n+1} + \Delta(m\mathbf{U})_{fc,\tau} + V \bar{\rho}_{fc}^n g \quad (59)$$

$$\Delta(me)_{fc} = V n_c^n P_c^{n+1} \nabla^c \cdot \mathbf{U}_{f,FC}^* + \nabla^c \cdot \mathbf{q}_{fc}^n \quad (60)$$

399    The Lagrangian value of the mass, linear momentum and energy of fluid  
 400    phases without momentum exchange are:~

$$m_{fc}^L = V \bar{\rho}_{fc}^n \quad (61)$$

$$(m\mathbf{U})_{fc}^{L-} = V \bar{\rho}_{fc}^n \mathbf{U}_{fc}^n + \Delta(m\mathbf{U})_{fc} \quad (62)$$

$$(me)_{\underline{\text{fc}}\underline{\text{f.c}}}^{L-} = V \bar{\rho}_{\underline{\text{fc}}\underline{\text{f.c}}}^n T_{\underline{\text{fc}}\underline{\text{f.c}}}^n c_v + \Delta(me)_{\underline{\text{fc}}\underline{\text{f.c}}} \quad (63)$$

403 For the solid phase, the Lagrangian value of the linear momentum and energy  
404 of solid phase are:

$$m_{sc}^L = m_{sc}^n \quad (64)$$

$$(m\mathbf{U})_{sc}^{L-} = \sum S_{ci} m_{si}^n \mathbf{U}_{si}^{L-} + V(1 - n_c^n) \nabla^c P_{\textcolor{red}{fc}}^{n+1} \quad (65)$$

$$(me)_{sc}^{L-} = \sum_i S_{ci} m_{si}^n T_{si}^L c_v \quad (66)$$

<sup>407</sup> To consider the momentum exchange, the Lagrangian velocity is modified as:

$$\begin{aligned} \mathbf{U}_{\underline{\mathbf{f}}\underline{\mathbf{c}}\underline{\mathbf{L}}\underline{\mathbf{c}}}^L &= \mathbf{U}_{\underline{\mathbf{f}}\underline{\mathbf{c}}\underline{\mathbf{L}}\underline{\mathbf{c}}}^{L-} + \Delta \mathbf{U}_{\underline{\mathbf{f}}\underline{\mathbf{c}}\underline{\mathbf{L}}\underline{\mathbf{c}}} \\ \mathbf{U}_{sc}^L &= \mathbf{U}_{sc-}^{L-} + \Delta \mathbf{U}_{sc} \end{aligned} \quad (67)$$

where the cell-centered intermediate velocity can be calculated by:

$$U_{\underline{\underline{fc}}\underline{\underline{sc}}} = \frac{(mU)_{fc}^{L-}}{m_{fc}^L} \frac{(mU)_{f,c}^{L-}}{m_{f,c}^L}$$

$$U_{sc}^{L-} = \frac{(mU)_{sc}^{L-}}{m_{sc}^L} \quad (68)$$

410 And the increment of the velocity  $\dot{\mathbf{U}}_{f\text{c}} - \dot{\mathbf{U}}_{l\text{c}}$ ,  $\Delta \mathbf{U}_{sc}$  can be computed by solving  
 411 the linear equation with  $i,j = 1 : N$  as:

$$\begin{vmatrix} (1 + \beta_{ij}) & -\beta_{ij} \\ -\beta_{ji} & (1 + \beta_{ji}) \end{vmatrix} \begin{vmatrix} \Delta U_{i,c} \\ \Delta U_{j,c} \end{vmatrix} = \begin{vmatrix} \beta_{ij}(U_{i,c}^{*\text{L-}} - U_{j,c}^{*\text{L-}}) \\ \beta_{ji}(U_{j,c}^{*\text{L-}} - U_{i,c}^{*\text{L-}}) \end{vmatrix}$$

To consider the energy exchange, the Lagrangian temperature is modified as:

$$T_{\underline{\text{fc}}\underline{\text{Lc}}}^L = T_{\underline{\text{fc}}\underline{\text{Lc}}}^{L-} + \Delta T_{\underline{\text{fc}}\underline{\text{Lc}}} \quad (69)$$

414 where the cell-centered intermediate temperature can be calculated by:

$$T_{\underline{fc}\underline{f}\underline{c}}^{L-} = \frac{(mT)_{fc}^{L-}}{\underline{m_{fc}^L c_v}} \frac{(mT)_{f,c}^{L-}}{\underline{m_{f,c}^L c_v}} \quad (70)$$

$$T_{sc}^{L-} = \frac{(mT)_{sc}^{L-}}{m_{sc}^L c_v}$$

415 And the increment of the velocity can be computed by solving the linear  
 416 equation with  $i,j = 1 : N$  as:

$$\begin{vmatrix} (1 + \eta_{ij}) & -\eta_{ij} \\ -\eta_{ji} & (1 + \eta_{ji}) \end{vmatrix} \begin{vmatrix} \Delta T_{i,c} \\ \Delta T_{j,c} \end{vmatrix} = \begin{vmatrix} \eta_{ij}(T_{i,c}^{\text{nL}} - T_{j,c}^{\text{nL}}) \\ \eta_{ji}(T_{j,c}^{\text{nL}} - T_{i,c}^{\text{nL}}) \end{vmatrix}$$

417 Finally, we obtain the cell-centered solid acceleration and temperature rate  
 418 as: $\ddot{\cdot}$

$$d\mathbf{U}_{sc}^L = \frac{(m\mathbf{U})_{sc}^L - (m\mathbf{U})_{sc}^n}{m_{sc}^L \Delta t} \quad (71)$$

$$dT_{sc}^L = \frac{(me)_{sc}^L - (me)_{sc}^n}{m_{sc}^L c_v \Delta t} \quad (72)$$

420 *Compute Lagrangian specific volume of the fluid phase*

421 To compute the Lagrangian value of the specific volume of the fluid phase,  
 422 we need to compute the Lagrangian temperature rate as below: $\dot{\cdot}$

$$T_{fc}^{n+1} = \frac{(me)_{fc}^L}{m_{fc}^L c_v} \frac{(me)_{f,c}^L}{\tilde{m}_{f,c}^L c_v} \quad (73)$$

$$\frac{D_f T_{fc}}{Dt} \frac{D_f T_{f,c}}{Dt} = \frac{T_{fc}^{n+1} - T_{fc}^n}{\Delta t} \frac{T_{f,c}^{n+1} - T_{f,c}^n}{\Delta t} \quad (74)$$

424 As such, the Lagrangian specific volume rate is:

$$\Delta(mv)_{fc}^{\phi} = V f_{fc}^{\phi} \nabla \cdot \mathbf{U} + (\phi_{fc} \alpha_{fc} \frac{D_f T_{fc}}{Dt} \frac{D_f T_{f,c}}{Dt} - f_{fc}^{\phi} \sum_{n=1}^N \phi_{nc} \alpha_{nc} \frac{D_n T_{nc}}{Dt} \frac{D_n T_{n,c}}{Dt}) \quad (75)$$

425 where  $f_f^{\phi} = (\phi_f \kappa_f) / (\sum_{n=1}^N \phi_n \kappa_n)$  and  $\mathbf{U} = \nabla \cdot (\sum_{s=1}^{N_s} \phi_{sc} \mathbf{U}_{sc} + \sum_{f=1}^{N_f} \phi_{fc} \mathbf{U}_{fc})$   
 426 Finally, the Lagrangian specific volume is: $\ddot{\cdot}$

$$(mv)_{fc}^L = V \bar{\rho}_{f,c}^n v_{fc}^n + \Delta(mv)_{fc}^{\phi} \quad (76)$$

427    *Compute advection term and advance in time*

428    The time advanced mass, linear momentum, energy and specific volume  
429    are:

$$430 \quad m_{\underline{fc}\underline{f},c}^{n+1} = m_{\underline{fc}\underline{f},c}^L - \Delta t \nabla \cdot (\bar{\rho}_{\underline{fc}\underline{f},c}^L, \mathbf{U}_{f,FC}^L) \quad (77)$$

$$431 \quad (m\mathbf{U})_{\underline{fc}\underline{f},c}^{n+1} = (m\mathbf{U})_{\underline{fc}\underline{f},c}^L - \Delta t \nabla \cdot ((\bar{\rho}\mathbf{U})_{\underline{fc}\underline{f},c}^L, \mathbf{U}_{f,FC}^L) \quad (78)$$

$$432 \quad (me)_{\underline{fc}\underline{f},c}^{n+1} = (me)_{\underline{fc}\underline{f},c}^L - \Delta t \nabla \cdot ((\bar{\rho}c_v T)_{\underline{fc}\underline{f},c}^L, \mathbf{U}_{f,FC}^L) \quad (79)$$

$$433 \quad (mv)_{\underline{fc}\underline{f},c}^{n+1} = (mv)_{\underline{fc}\underline{f},c}^L - \Delta t \nabla \cdot ((\bar{\rho}v)_{\underline{fc}\underline{f},c}^L, \mathbf{U}_{f,FC}^L) \quad (80)$$

434    Finally, the state variables of the fluid phases of the next time step are: $\sim$

$$435 \quad \bar{\rho}_{\underline{fc}\underline{f},c}^{n+1} = \frac{m_{fc}^{n+1}}{\underline{V}} \frac{m_{f,c}^{n+1}}{\underline{V}} \quad (81)$$

$$436 \quad \mathbf{U}_{\underline{fc}\underline{f},c}^{n+1} = \frac{(m\mathbf{U})_{fc}^{n+1}}{\underline{m_{fc}^{n+1}}} \frac{(m\mathbf{U})_{f,c}^{n+1}}{\underline{m_{f,c}^{n+1}}} \quad (82)$$

$$437 \quad T_{\underline{fc}\underline{f},c}^{n+1} = \frac{(me)_{fc}^{n+1}}{\underline{m_{fc}^{n+1}}} \frac{(me)_{f,c}^{n+1}}{\underline{m_{f,c}^{n+1}}} \quad (83)$$

$$438 \quad v_{\underline{fc}\underline{f},c}^{n+1} = \frac{(mv)_{fc}^{n+1}}{\underline{m_{fc}^{n+1}}} \frac{(mv)_{f,c}^{n+1}}{\underline{m_{f,c}^{n+1}}} \quad (84)$$

439    *Interpolate from cell to node of the solid phase*

440    First we interpolate the acceleration, velocity and temperature rate to  
441    the node as below:

$$442 \quad \mathbf{a}_{si}^n = \sum S_{ci} d\mathbf{U}_{sc}^L \quad (85)$$

$$443 \quad \mathbf{U}_{si}^{n+1} = \sum S_{ci} d\mathbf{U}_{sc}^L \Delta t \quad (86)$$

$$444 \quad dT_{si}^n = \sum S_{ci} dT_{sc}^L \quad (87)$$

445    Then the boundary condition and contact forces  $f_{si}^{fric}$  are applied to the nodal  
446    velocity and the acceleration is modified by: $\sim$

$$447 \quad \mathbf{a}_{si}^n = \frac{\mathbf{v}_{si}^{n+1} - \mathbf{v}_{si}^n}{\Delta t} \quad (88)$$

444    *Update the particle variables*

445    The state variables of the solid phase [ $\mathbf{U}_{sp}^{n+1}, \mathbf{x}_{sp}^{n+1}, \nabla \mathbf{U}_{sp}^{n+1}, T_{sp}^{n+1}, \nabla T_{sp}^{n+1}, \mathbf{F}_{sp}^{n+1}, V_{sp}^{n+1}$ ]  
 446    (velocity, position, velocity gradient, temperature, temperature gradient, de-  
 447    formation gradient, volume) are updated [here](#) as:

$$\mathbf{U}_{sp}^{n+1} = \mathbf{U}_{sp}^n + \sum S_{sp} \mathbf{a}_{si}^n \Delta t \quad (89)$$

$$\mathbf{x}_{sp}^{n+1} = \mathbf{x}_{sp}^n + \sum S_{sp} \mathbf{U}_{si}^{n+1} \Delta t \quad (90)$$

$$\nabla \mathbf{U}_{sp}^{n+1} = \sum \nabla S_{sp} \mathbf{U}_{si}^{n+1} \quad (91)$$

$$T_{sp}^{n+1} = T_{sp}^n + \sum S_{sp} dT_{si}^n \Delta t \quad (92)$$

$$\nabla T_{sp}^{n+1} = \sum \nabla S_{sp} T_{sp}^n \Delta t \quad (93)$$

$$\mathbf{F}_{sp}^{n+1} = (\mathbf{I} + \nabla \mathbf{U}_{sp}^{n+1} \Delta t) \mathbf{F}_{sp}^n \quad (94)$$

$$V_{sp}^{n+1} = \det(\mathbf{F}_{sp}^{n+1}) V_{sp}^o \quad (95)$$

454    Finally, the effective stress  $(\sigma')^{n+1}$  is updated from the constitutive model  
 455    and the pore water pressure is interpolated from the cell as:

$$p_f^{n+1} = \sum S_{si} P_c^{n+1} \quad (96)$$

## 456    Numerical examples

457    All input files and the analytical calculations in this section are provided  
 458    in the Github repository ([https://github.com/QuocAnh90/Uintah\\_NNTU](https://github.com/QuocAnh90/Uintah_NNTU))  
 459    for the reproduction of the numerical results.

460    To prevent repetition, we present the parameters of water and air, which  
 461    remain consistent across all simulations. The water has a bulk modulus of 2  
 462    GPa, a density of 998 kg/m<sup>3</sup> at a reference temperature of 5 degrees Celsius  
 463    and a reference pressure of 10325 Pa (1atm), a dynamic viscosity  $\mu_f$  of 1  
 464    mPa s). The air has a ideal gas with a density of 1.17 kg/m<sup>3</sup> at a reference  
 465    temperature of 5 degrees Celsius and a reference pressure of 10325 Pa (1atm),  
 466    a dynamic viscosity  $\mu_f$  of  $18.45E^{-3}$  mPa s).

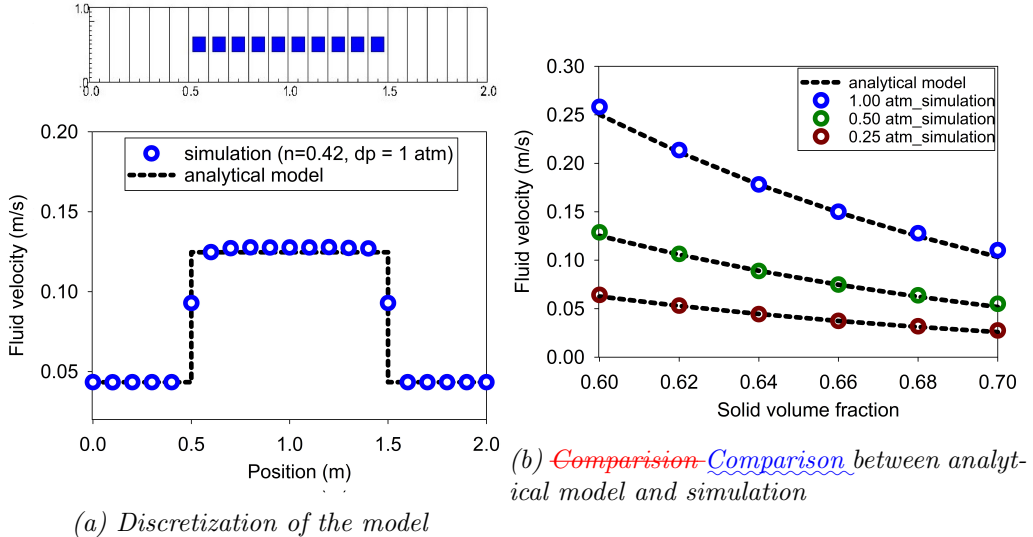


Figure 7: Numerical results of the fluid flow through isothermal porous media

#### 467 Fluid Flow through isothermal porous media

468 Fluid flow through porous media is important in many engineering disciplines,  
469 like predicting water flow in soil. Fluid flow velocity in one dimension  
470 can be calculated from the porous media's hydraulic conductivity  $K$  as:

471

$$U_f = K \frac{\Delta p_f}{L} \quad (97)$$

472 If the Carman-Kozeny formula is adopted  $F = 10\phi_s/(1 - \phi_s)^2$ , the hydraulic  
473 conductivity will be expressed as  $K = d^2(1 - \phi_s)^3 / 180\mu\phi_s^2$ . Then, the analytical formula of average velocity in one dimension through  
474 the porous media is:  
475

476

$$U_f = \frac{1}{n} \frac{d^2(1 - \phi_s)^3}{180\mu\phi_s^2} \frac{D_p^2(1 - \phi_s)^3}{180\phi_s^2\mu_f} \frac{\Delta p_f}{L} \quad (98)$$

477 Our numerical model is validated by modeling fluid flow through a 1m  
478 long porous media. This fluid has water properties (bulk modulus is 2GPa,  
479 density is 998 kg/m<sup>3</sup> at 5 degrees Celsius and 10325 Pa (1atm) pressure,  
480 dynamic viscosity  $\mu$  is 1mPa s). The porous media is modeled by elastic  
481 material with Young's modulus is 10 MPa, Poisson's ratio is 0.3, and density  
482 is 2650 kg/m<sup>3</sup>. The volume fraction of porous media  $\phi_s$  is [0.6, 0.62, 0.66,

483 0.68, 0.7] and the average grain diameter  $d$  is 1mm. The model is discretized  
 484 in 20 finite element and the porous media in 10 finite element with 1 material  
 485 point per element. The pressure gradient is applied with three different value  
 486 [0.25, 0.5, 1] atm. Figure 7 shows a good agreement of fluid flow prediction  
 487 between the theory and the model.

488 *Isothermal consolidation*

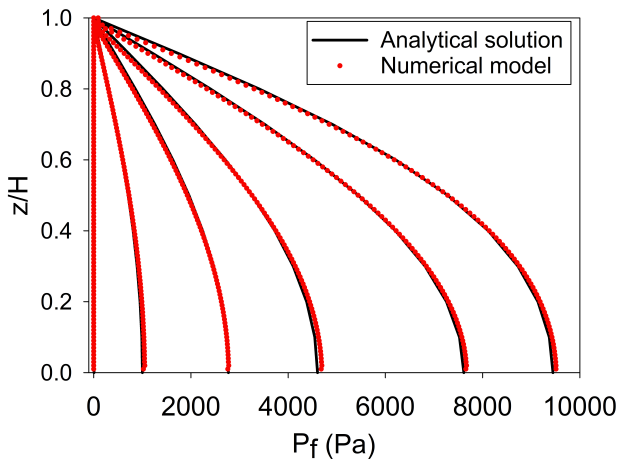


Figure 8: Comparison between analytical solution and numerical solution

489 A common benchmark ~~for~~ for a fully saturated porous ~~meida~~~~media~~ is  
 490 the simulation of one-dimensional consolidation. Using the Carman-Kozeny  
 491 formula, the time-dependent pressure can be ~~evaluated~~~~calculated~~ as:

$$p_f = \sum_{m=1}^{\infty} \frac{2F_{ext}}{M} \sin\left(\frac{Mz}{H}\right) e^{-M^2 T_v} \text{ with } M = \frac{\pi}{2}(2m + 1) \quad (99)$$

492 where the consolidation rate  $T_v = C_v t / H^2$ , the consolidation coefficient  $C_v =$   
 493  $E_v n^3 d^2 / (180(1 - n)^2 \mu)$  and the Oedometer modulus  $E_v = E(1 - v) / (1 +$   
 494  $v) / (1 - 2v)$ . Our numerical model is validated by modeling the consolidation  
 495 of a 1m column. ~~This fluid has water properties (bulk modulus is 2GPa,~~  
 496 ~~density is 998 kg/m3 at 5 degrees Celsius and 101325 Pa (1atm) pressure,~~  
 497 ~~dynamic viscosity  $\mu$  is 1mPa s).~~ The porous media is modeled by elastic  
 498 material with Young's modulus is 10 MPa, Poisson's ratio is 0.3, and density  
 499 is 2650 kg/m3. The volume fraction of porous media  $\phi_s$  is 0.7 which is

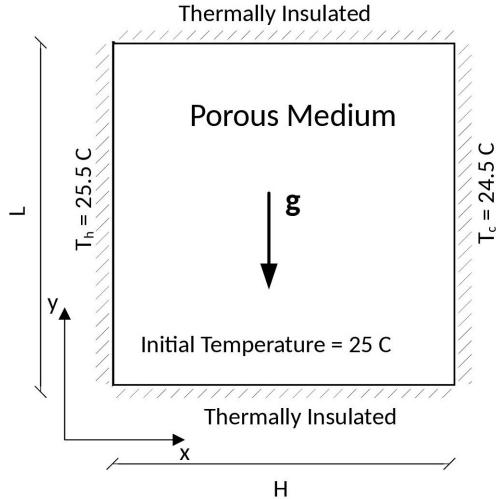


Figure 9: Model schematic [23]

500 equivalent to the porosity of 0.3 and the average grain diameter  $d$  is 1mm.  
 501 The model is discretized in 100 finite element with 1 material point per  
 502 element. The external pressure applies to the top of the column is 10 kPa.  
 503 Figure 8 shows a good agreement of fluid flow prediction between the theory  
 504 and the model.

505 *Thermal induced cavity flow*

506 Another ~~benchmark~~ is the thermal induced cavity flow in  
 507 porous media. Temperature and velocity distributions are calculated for a  
 508 square non-deformable saturated porous media. The top and bottom walls  
 509 are insulated, and the left and right walls are at fixed ~~temperatures differing~~  
 510 ~~by temperature gradient of~~ 1 degree. The fluid motion at steady state are  
 511 cavity flow due to the temperature induced density variation. The numerical  
 512 is validated by comparing with the numerical solution of the finite element  
 513 method. The ~~fluid has water properties (bulk modulus is 2GPa, density is 998~~  
 514 ~~kg/m3 at 5 degrees Celsius and 10325 Pa (1atm) pressure, dynamic viscosity~~  
 515 ~~μ is 1 mPa s~~). The porous media is modeled by non deformable material,  
 516 and density is 2500 kg/m<sup>3</sup>. The specific heat capacity of the water and  
 517 porous skeleton are 4181 J/kg.K and 835 J/kg.K respectively. The thermal  
 518 conductivity of the water and porous skeleton are 0.598 W/m.K and 0.4  
 519 W/m.K. The volume fraction of porous media  $\phi_s$  is 0.6 which is equivalent

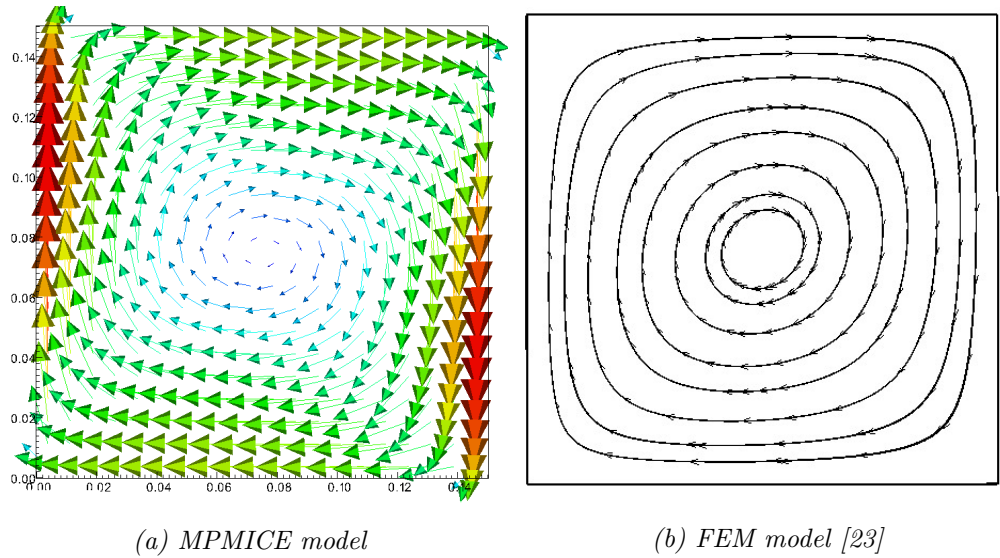


Figure 10: ~~Comparision~~ Comparison between MPMICE model and FEM model

520 to the porosity of 0.4 and the average grain diameter  $d$  is 1mm. The model is  
 521 discretized in  $20 \times 20$  finite element with 4 material point per element. Figure  
 522 10 shows a good agreement of numerical results of the model compared with  
 523 the numerical solution of the finite element method.

524 *Underwater debris flow*

525 The numerical example is validated ~~by using the experimental work of~~  
 526 Rzadkiewicz et al. ~~'s experiment~~ on submarine debris flow [24]. ~~During~~  
 527 ~~the~~In their experiment, sand ~~in~~within a triangular box is released and ~~then~~  
 528 slides along a rigid bed inclined ~~at~~ 45 degrees under water ~~, (see Figure 11-0.4~~  
 529 ~~seconds subfigure 0.8 seconds subfigure~~Simulation of underwater debris flow  
 530 ~~figure~~Materials Bulk modul(Pa)~~tabular~~ Shear modul(Pa)~~tabular~~ Density(kg/m<sup>3</sup>)~~tabula~~  
 531 Temp(C)~~tabular~~ Dynamic viscosity(Pa s)~~tabular~~ Yield stress(Pa)~~tabular~~  
 532 ~~Water(at surface)~~tabular ~~2.15e9 - 999.8~~ ~~5.855e-6 - Air(at top boundary)~~tabular  
 533 ~~-1.177 5 18.45e-6 - Sand(porous media)~~tabular ~~8.33e6 20e6 1985 5 - 200 Rigid~~  
 534 ~~bed(solid)~~tabular ~~117e7 43.8e7 8900 5 -- tabular~~Numerical parameters for the  
 535 ~~underwater submarine debris tableIn~~). The material properties in the nu  
 536 ~~merical model , the material properties~~ are selected based on the experiment  
 537 by Rzadkiewicz et al[24]. ~~Sand has . [24]. The sand is characterized by a~~  
 538 ~~saturated density of 1985 kg/m<sup>3</sup> and yield stress of 200 Pa. a friction angle~~

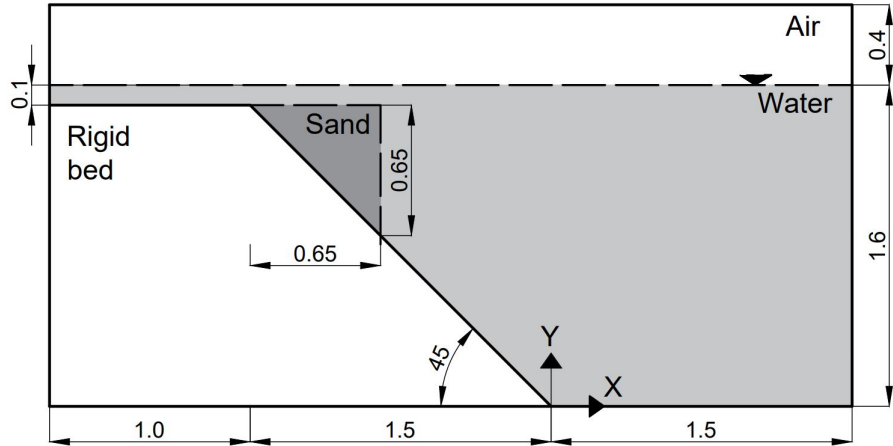


Figure 11: Model schematic

539 of 10 degrees. The effect of Young's modulus has little effect on debris flow  
 540 run-out because of the extreme large is negligible due to the extreme deformation of the debris. Therefore, we select 50 MPa, so a Young's modulus  
 541 with 0.25 of 50 MPa with a Poisson's ratio of 0.25 is chosen. The rigid bed is  
 542 much stiffer with being much stiffer, has bulk modulus and shear modulus  
 543 values of  $117E^7$  Pa and  $43.8E^7$  Pa. Under gravity, the density of the water  
 544 at the surface is  $999.8 \text{ kg/m}^3$  at the pressure of 1 atm. At the top boundary,  
 545 the air has a density of  $1.17 \text{ kg/m}^3$  at the atmospheric pressure of 1 atm.  
 546 At 5 Celsius degrees, air and water have viscosity of  $18.45E^{-3}$  mPa s and  
 547  $1 \text{ mPa s}$ , respectively. The numerical parameters used in this example are  
 548 presented in Table 1.

549 On The boundary conditions imposed in the numerical model are as follows:  
 550 on all boundary faces, the Dirichlet boundary condition is imposed for velocity  
 551 ( $u$  velocity is set to zero ( $U = 0 \text{ m/s}$ ) and temperature the temperature is  
 552 set to 5 degrees Celsius ( $T = 5 \text{ Celsius degrees}$ ), while the Neuman boundary  
 553 condition is imposed at the top boundary for pressure ( $^\circ\text{C}$ ). At the top boundary,  
 554 the pressure has a Neumann boundary condition of  $dp/dx = 0 \text{ kPa}$ ) and  
 555 density (, and the density has a Neumann boundary condition of  $d\rho/dx =$   
 556  $0 \text{ kg/m}^3$ ). For the background mesh , there are . The background mesh  
 557 consists of  $700 \times 400 = 280,000$  cells. In each cell of cells, resulting in a total  
 558 of 280,000 cells. Each cell in the debris flow and rigid bed , there are contains  
 559 2 x 2 material points.

560 0.4 seconds subfigure0.8 seconds subfigureSimulation of underwater debris

562 flow figureFigure ?? and ?? show Figure 13b illustrates snapshots of the  
563 underwater debris flow sliding in the plane at 0.4 s and 0.8 s. Our simulations  
564 match the computed results from Rzadkiewicz et al. [24]. The model also  
565 captures, demonstrating that the model captures the typical hydroplaning  
566 mechanism of the underwater debris flow(hydroplaning means the debris  
567 flow is lifted up and no longer in . Hydroplaning refers to the lifting of the  
568 debris flow, causing it to lose contact with the bottom layer). The elevation  
569 of the free surface at 0.4s and 0.8s is compared between our proposed  
570 method and other methods in Figure 12. Once again, our computed results  
571 were consistent with both the experiment and others computational Our  
572 computed results align well with the experimental results [7].  
573 Unlike other computational models based that rely on total stress analysis  
574 , the proposed model based on the [5, 6, 7, 8], our proposed model utilizes  
575 effective stress analysiswhich allows to analyze the , enabling the analysis  
576 of water pressure and temperature in within the debris flow. saturated  
577 debris flow using MPM subfigureunderwater debris flow using MPMICE  
578 subfigureSimulation of underwater debris flow figureWe also explore the difference  
579 Additionally, we investigate the differences between underwater debris flow  
580 and saturated debris flow in terms of interacting with obstacletheir interaction  
581 with obstacles. Figure 13 shows the snapshot of the simulations of presents  
582 snapshots of simulations of both underwater and saturated debris flow. The  
583 saturated debris flow (see Figure 13a) behaves like frictional flowas grain  
584 exhibits behavior similar to frictional flow, where grains have contact forces  
585 with each other. On the other handConversely, the underwater debris flow  
586 (see Figure 13b) behaves like turbulent flowas grains are turbulent flow, with  
587 grains being separated from each other and exhibit exhibiting no contact  
588 forces between grains. (as reflected by the near-zero effective stress in the  
589 turbulence domain).

Materials	Bulk modul (Pa)	Shear modul (Pa)	Density (kg/m <sup>3</sup> )	Temp (C)	Dynamic viscosity (Pa s)	Friction angle (degrees)
Water (at surface)	2.15e9	-	999.8	5	855e-6	-
Air (at top boundary)	-	-	1.177	5	18.45e-6	-
Sand (porous media)	8.33e6	20e6	1985	5	-	10
Rigid bed (solid)	117e7	43.8e7	8900	5	-	-

Table 1: Numerical parameters for the underwater submarine debris

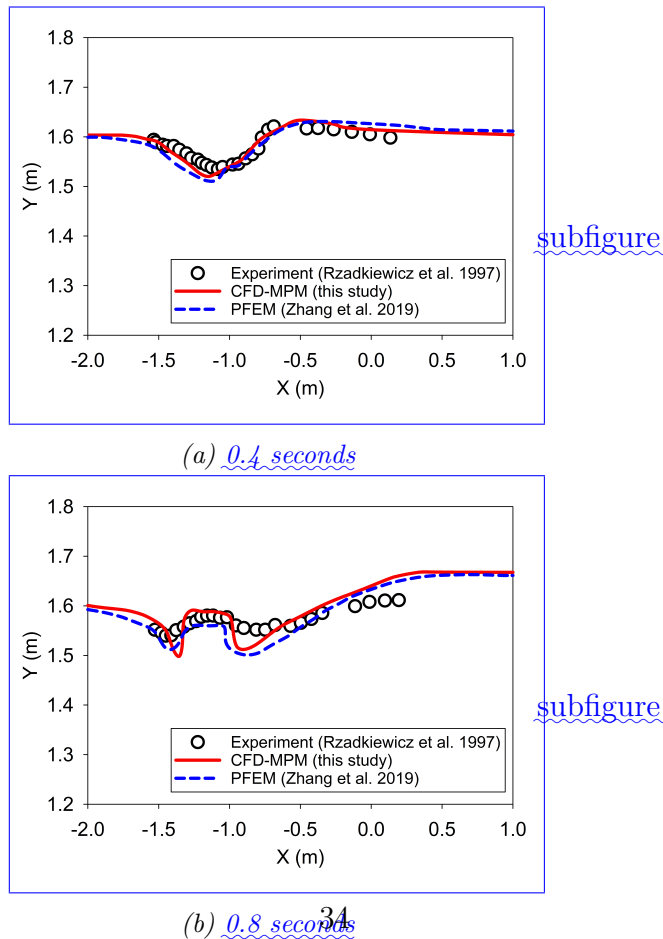


Figure 12: Evolution of water level in the simulation of underwater debris flow

590        figure

591        Validation of soil response to the seismic loading

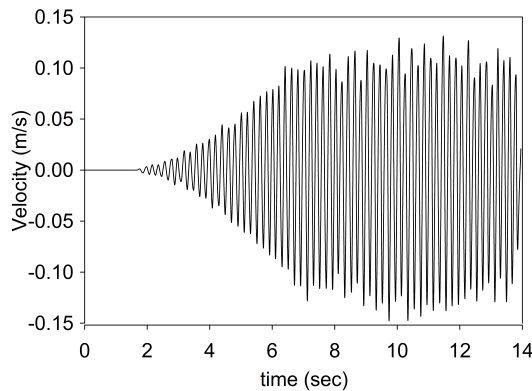


Figure 14: Seismic loading

592        figure

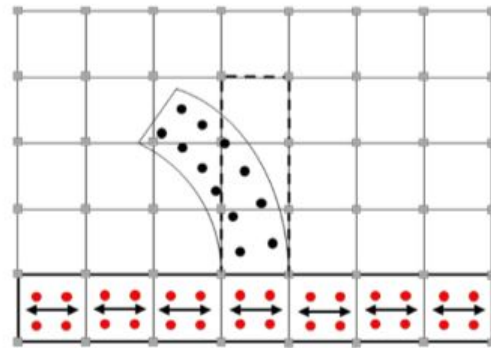
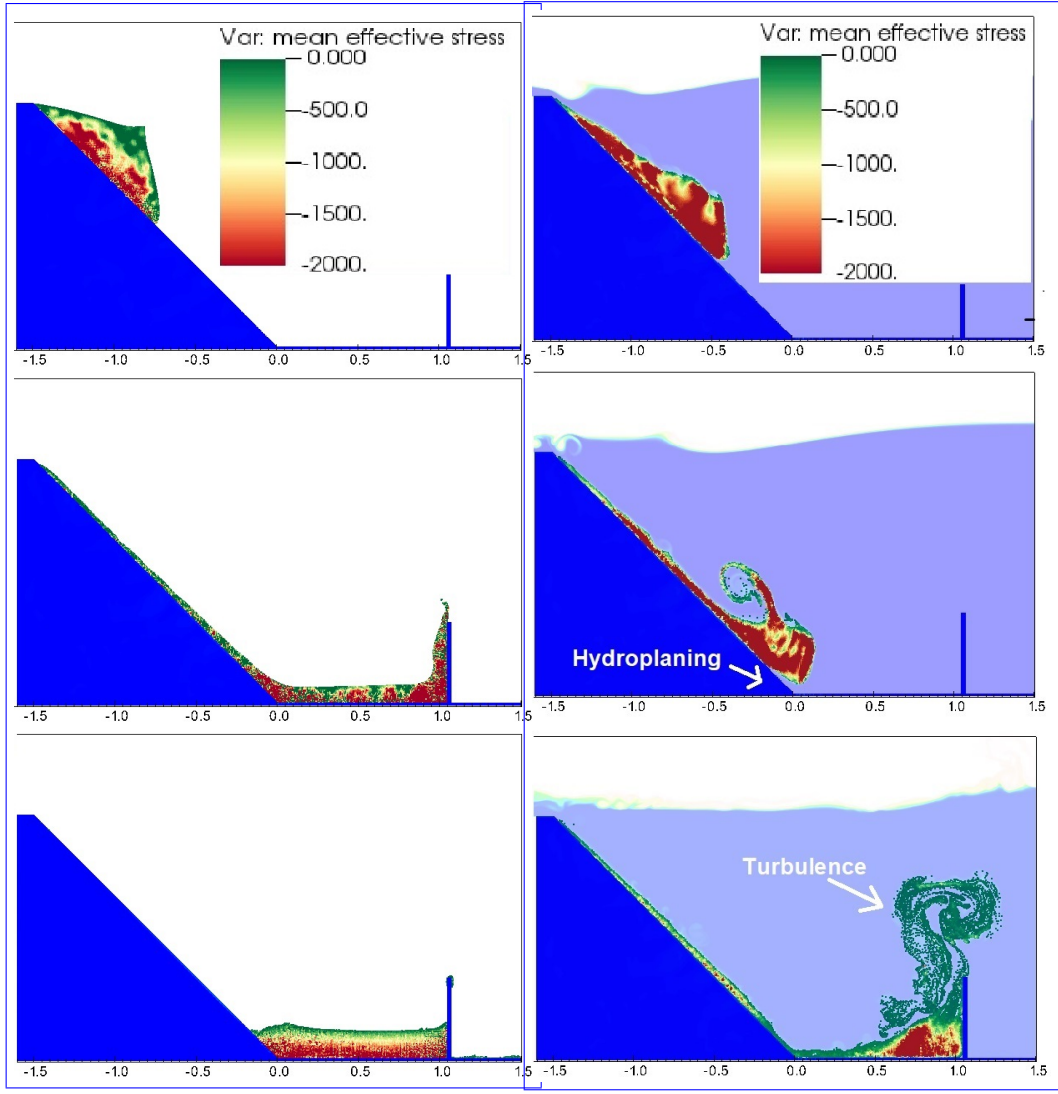


Figure 15: Material points prescribed velocity as kinematic boundary condition [25]

593        figure An experimental study conducted by Hiraoka et al. [26] aimed to  
594        investigate the influence of seismic shaking on the deformation of a 0.5 m-high  
595        sand slope. The sand used in the experiment was partially saturated, with a  
596        moisture content of 10 percent. The provided soil parameters for the Mohr  
597        Coulomb model include the effective friction angle of 23 degrees, apparent  
598        cohesion of 0.78 kPa, Young's modulus of 2.57 MPa, and Poisson's ratio of



(a) saturated debris flow using MPM      (b) underwater debris flow using MPMICE

*Figure 13: Simulation of Debris Flow: Mean Effective Stress Distribution (Green Color Indicates Near-Zero Effective Stress)*

599 0.33, and moist unit weight of 16.5 kN/m<sup>3</sup>. The soil's dilatancy angle was  
 600 assumed to be 0 [26]. The experimental setup consisted of a shaking table  
 601 box with a steel horizontal base and smooth glass vertical sidewalls. Laser  
 602 sensors were used to monitor the displacement of the slope's toe and crest.  
 603 Figure 14 displays the velocity-time history employed in the experiment.

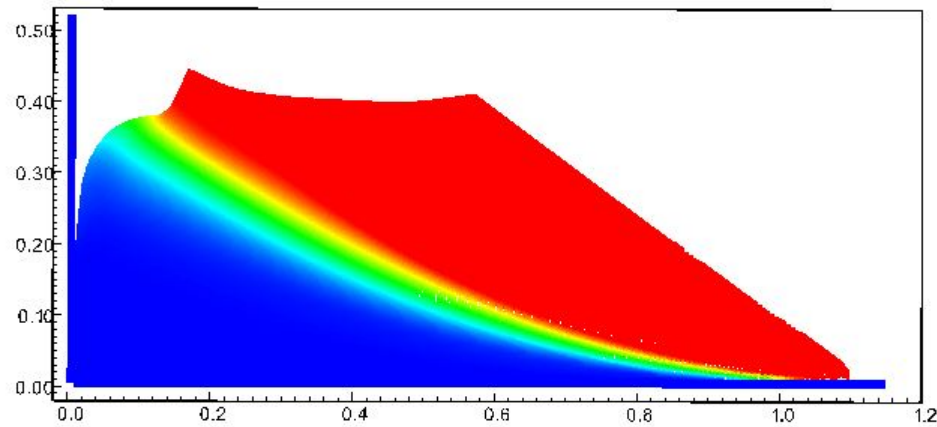


*Figure 16: Numerical model of the seismic-induced slope failure with displacement color*

604 figure

605 To simulate the seismic loading in our numerical model, we adopted a  
 606 method presented by Alsardi et al. [25], which involves specifying the velocity  
 607 at the corresponding material points representing either the shaking table or  
 608 the bedrock at the site (see Figure 15). In our simulation, we considered the  
 609 horizontal base to be fully rough and the vertical contact to be fully smooth.  
 610 The initial stress condition was initiated using gravity and seismic loading  
 611 induced the slope failure (see Figure 16).  
 612 Previous studies by Bhandari et al. [27], Alsardi et al. [25], and Hiraoka et  
 613 al. [26] attempted to model this experiment using MPM and SPH models. In  
 614 this study, we compared our results with those obtained from other particle-based  
 615 methods (Figure 17). The main difference is that we did not apply 5 percent  
 616 numerical damping in our model, unlike the other methods. We found  
 617 that the final displacement of the slope toe in our MPM model was higher  
 618 than that observed in the experiment. Nevertheless, the validation of the  
 619 Mohr-Coulomb model under seismic response demonstrated a reasonable soil  
 620 behavior in terms of displacement.

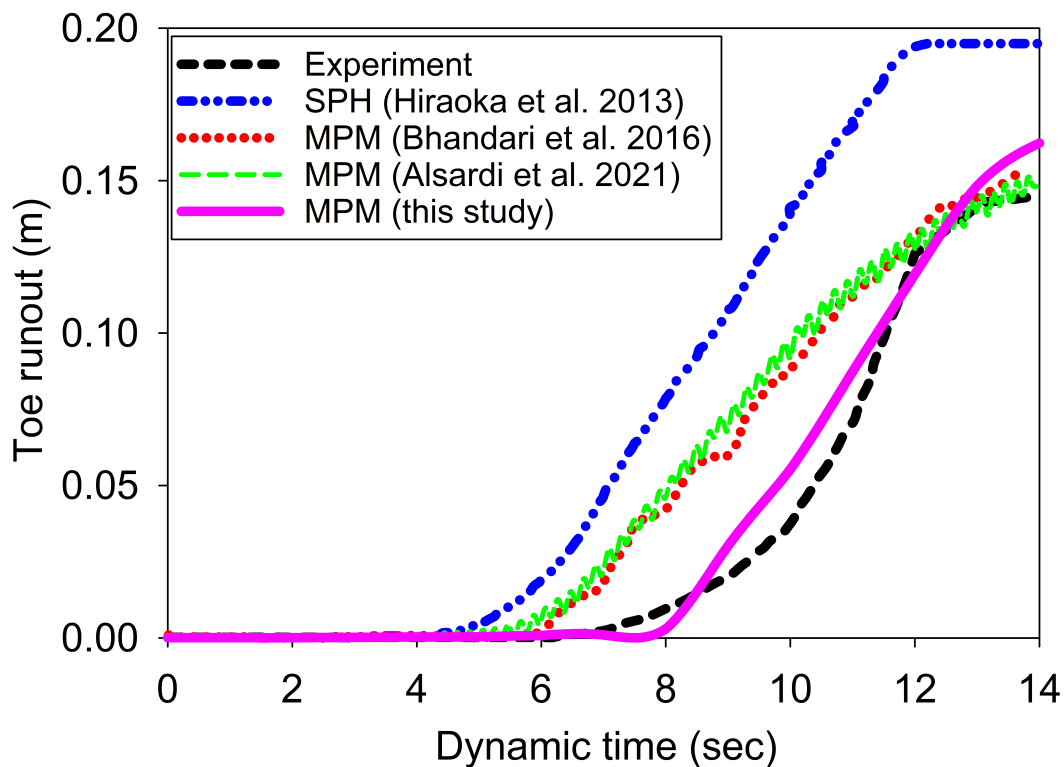


Figure 17: Displacement of the toe of the slope

621 [figure](#)

622 [Earthquake-induced submarine landslides](#)

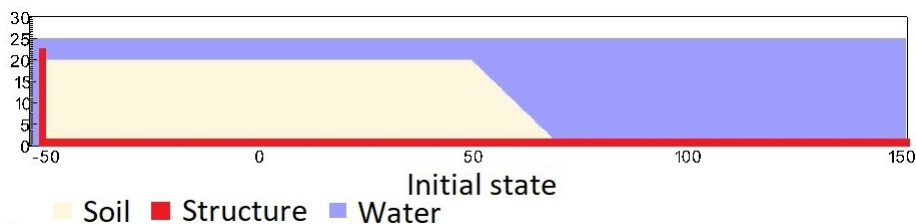


Figure 18: Numerical model simulation of the earthquake-induced submarine land-slide

623 [figure](#)

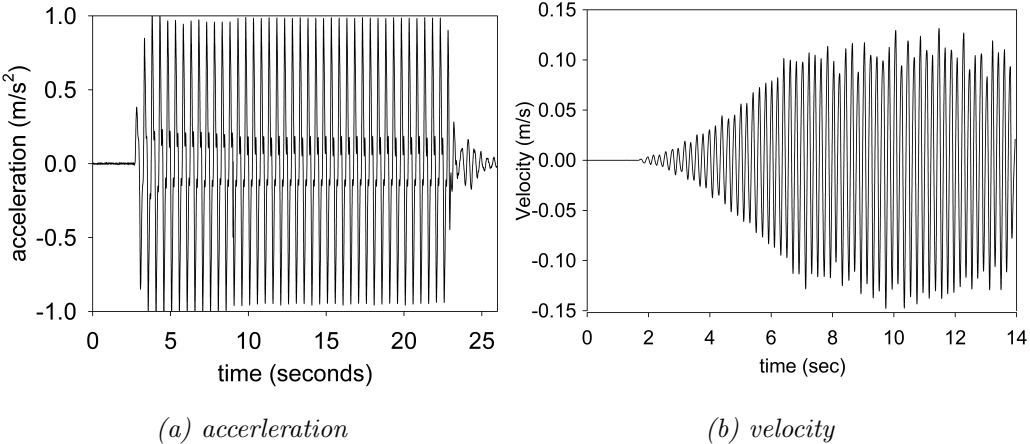


Figure 19: Ground acceleration profile, frequency of 2Hz and magnitude of 1g

In the final example, we perform numerical analysis of the earthquake induced submarine landslides. A plane strain model with the slope under water is shown in Figure 18. A 20m high slope with slope gradient of 45 degrees is placed in a horizontal and vertical structure which was used to be a shaking table to apply earthquake loading. We simplify the earthquake loading by simulating the ground shaking for 20 seconds with the peak constant ground acceleration of 1g and the a constant frequency of 2Hz (Figure 19a). The ground motion is applied in terms of velocity (Figure 19b). The An earthquake of this magnitude can occurred typically for the earthquake of magnitude of more than 6. is possible. For instance, in the case of the 2023 Turkey-Syria Earthquake, significant ground shaking with peak ground acceleration exceeding 1g was observed at numerous locations. This serves as an example of the practical occurrence of such high levels of ground acceleration during seismic events. To generate the seismic loading, the same method was used as presented in the previous numerical example.

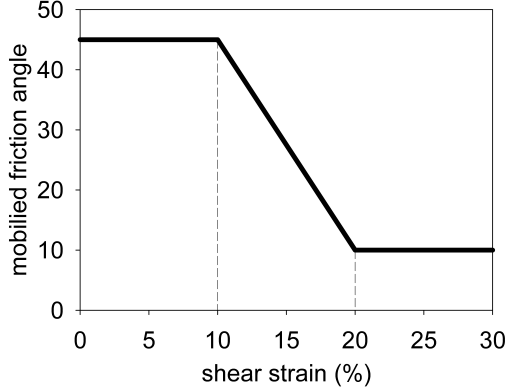


Figure 20: Mobilized friction angle in Mohr Coulomb model

639 A non-associated Mohr-Coulomb model is used for the soil. The soil grain  
 640 has the density of  $2650 \text{ kg/m}^3$ , Young's modulus of 10 kPa and Poisson's  
 641 ratio of 0.3 and zero cohesion. The mobilized friction angle  $\phi'_m$  is governed  
 642 following the softening curve (see Figure 20) with the peak friction angle  $\phi'_p$   
 643 of 45 degrees and the residual friction angle  $\phi'_r$  of 10 degrees. The porosity  
 644 is 0.3 and the average grain size of the soil is around  $0.1 \mu\text{m}$  to mimic the  
 645 undrained behavior. The mobilized dilatancy angle is calculated from the  
 646 ~~Rowe-stress dilatancy~~ [Rowe's stress dilatancy theory \[28\]](#) as follow:

$$\sin \psi'_m = \frac{\sin \phi'_m - \sin \phi'_r}{1 - (\sin \phi'_r \sin \phi'_m)} \quad (100)$$

647 The solid plane is modeled as a rigid body acted as a shaking table. The con-  
 648 tact between horizontal plane and the sand is the frictional contact with the  
 649 friction coefficient of 0.1. No artificial damping is applied in the simulation.  
 650 The contact between vertical plane and the sand is ~~eonsdered~~ [considered](#) to  
 651 be smooth with zero friction coefficient. ~~Under gravity, the density of the~~  
~~652 water at the surface is  $999.8 \text{ kg/m}^3$  at the pressure of 1 atm. At the top~~  
~~653 boundary, the air has a density of  $1.17 \text{ kg/m}^3$  at the atmospheric pressure~~  
~~654 of 1 atm. At 5 Celcius degrees, air and water have viscosity of  $18.45e^{-3} \text{ mPa}$~~   
~~655 s and 1 mPa s respectively.~~ On all boundary faces, the symmetric bound-  
 656 ary condition is imposed, while the ~~Neuman~~ [Neumann](#) boundary condition  
 657 is imposed at the top ~~boundaryfor~~ [boundary for](#) pressure ( $d\rho/dx = 0 \text{ kPa}$ )  
 658 and density ( $d\rho/dx = 0 \text{ kg/m}^3$ ). [Symmetric boundary condition refers to](#)  
~~a condition where the normal component of the velocity at the boundary~~

660 face is set to zero, and the tangential component is equal to the tangential  
 661 component of the neighboring cells. The mesh size is  $0.25 \times 0.25$ m with 300852  
 662 element cells and 142316 material points. The simulation takes a couple of  
 663 hours to perform 60 seconds of the simulation using 4096 CPUs.

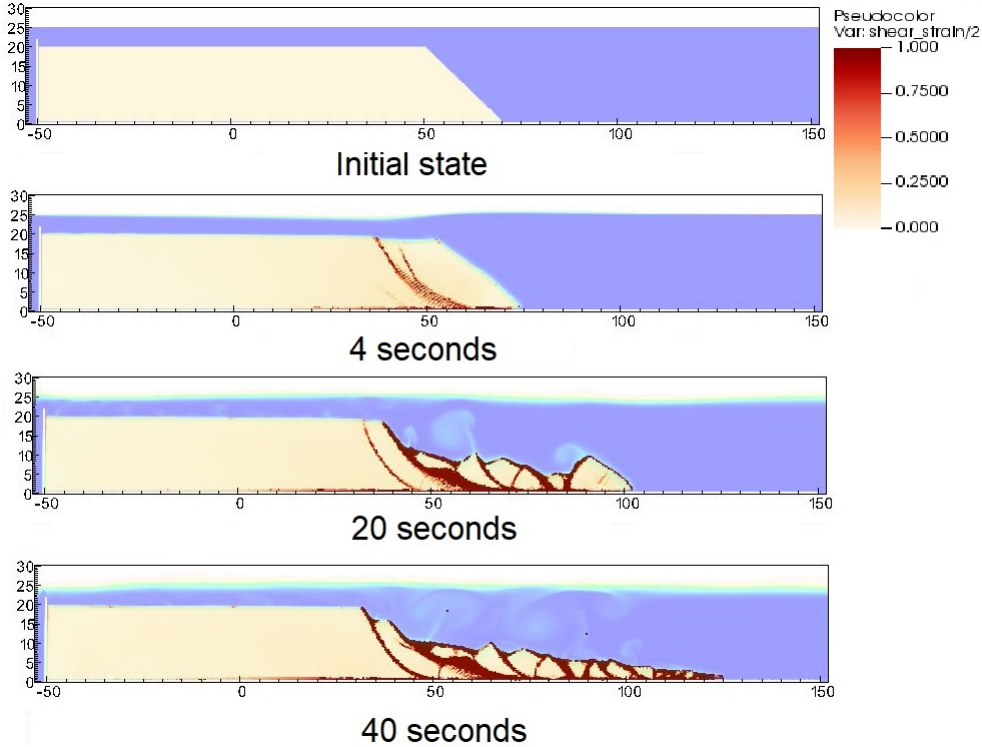


*Figure 21: Shear strain during the earthquake-induced submarine landslides*

664 We demonstrate the entire process and the mechanism of the earthquake-  
 665 induced submarine landslides by showing the shear strain (Figure 21), the  
 666 pore water pressure in atm (Figure 22) and the velocity (Figure 23).  
 667 The failure mechanism can be characterized as the progressive  
 668 failure mechanism. Here are some numerical observation:

- 669 1. At the initial of the seismic event, the seismic loading triggers the  
 670 first slide at 3 seconds. At 4 seconds, the debris start to move with the  
 671 maximum speed of around 2-3 m/s with multiple shear band developed  
 672 in the slope. The wave generated from the submarine slide is around  
 673 2-3m towards the slide direction.

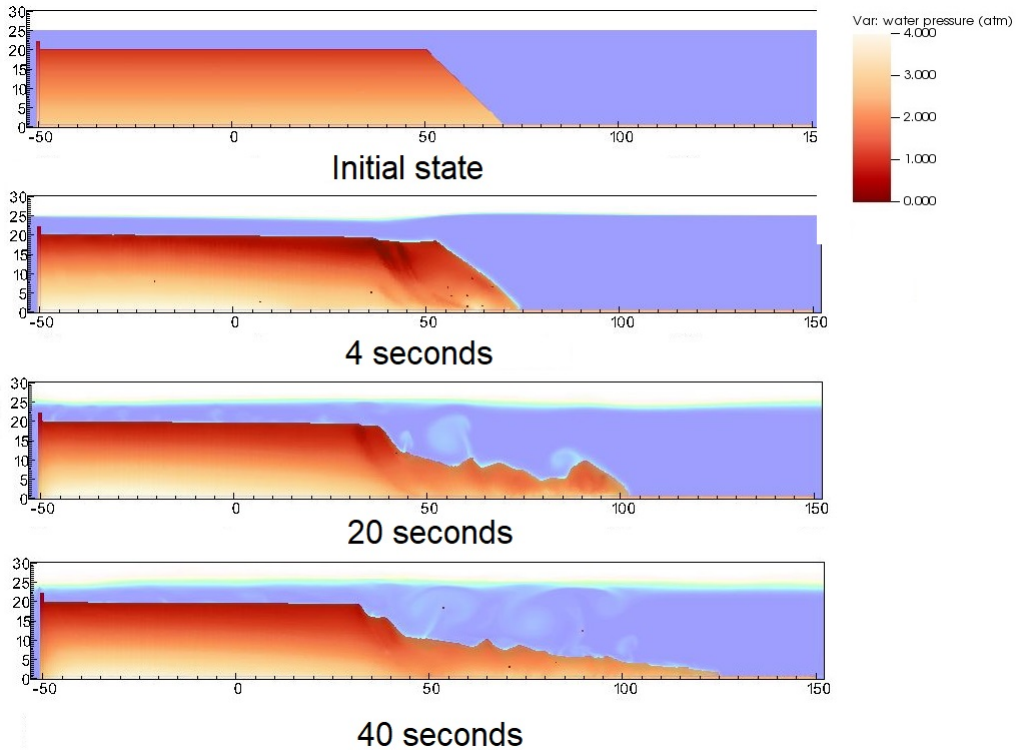


*Figure 22: pore water pressure during the earthquake-induced submarine landslides*

- 674     2. When the onset of the shear band occurs in the slope (for example  
 675       at 4 seconds and 20 seconds), the negative excess pore water pressure  
 676       is developed along this shear band with pore water pressure is under  
 677       1atm. This is a typical dilatancy behavior when the soil is sheared  
 678       rapidly in the undrained behavior.
- 679     3. When the seismic loading ends at 23 seconds, the last shear band is  
 680       mobilized and the slope soon reaches to the final deposition. No more  
 681       progressive failure developed in the slope. The turbulent flow developed  
 682       as the interaction between debris flow and seawater.
- 683     Overall, we show the completed process of the earthquake-induced submarine  
 684       landslides involving (1) earthquake triggering mechanism, (2) the onset of the  
 685       shear band with the development development of negative excess pore water  
 686       pressure, (3) progressive failure mechanism, (4) submarine landslide induced  
 687       wave to final deposition.

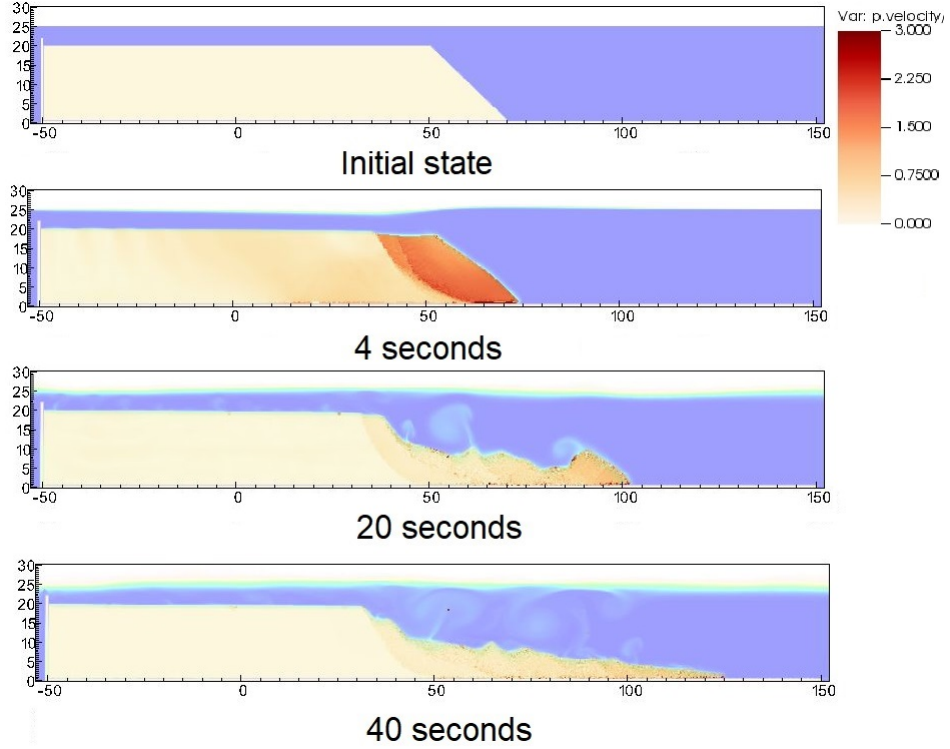


*Figure 23: Velocity during the earthquake-induced submarine landslides*

## 688      **Conclusions**

689      We have presented a numerical approach MPMICE for the simulation  
 690      of large deformation soil-fluid-structure interaction, emphasizing the simu-  
 691      lation of the earthquake-induced submarine landslides. The model uses (1)  
 692      the Material Point Method for capturing the large deformation of iso-thermal  
 693      porous media and solid structures and (2) Implicit Continuous Eulerian (com-  
 694      pressible, conservative multi-material CFD formulation) for modeling the  
 695      complex fluid flow including turbulence. This model is implemented in the  
 696      high-performance Uintah computational framework and validated against an-  
 697      alytical solution and experiment. We then demonstrate the capability of the  
 698      model to simulate the entire process of the earthquake induced submarine  
 699      landslides.

700 **Acknowledgements**

701 The authors gratefully acknowledge Dr. James Guilkey and Dr. Todd  
 702 Harman from the University of Utah for sharing the insight on the theoretical  
 703 framework of MPMICE which this work is based. This project has received  
 704 funding from the European Union's Horizon 2020 research and innovation  
 705 program under the Marie Skłodowska-Curie Actions (MSCA) Individual Fel-  
 706 lowship (Project SUBSLIDE "Submarine landslides and their impacts on  
 707 offshore infrastructures") grant agreement 101022007. The authors would  
 708 also like to acknowledge the support from the Research Council of Norway  
 709 through its Centers of Excellence funding scheme, project number 262644  
 710 Porelab. The computations were performed on High Performance Comput-  
 711 ing resources provided by UNINETT Sigma2 - the National Infrastructure  
 712 for High Performance Computing and Data Storage in Norway.

713 **Appendix: Equation derivation**

714 Before deriving the governing equation, we define the Lagrangian deriva-  
 715 tive for a state variable  $f$  as:

$$\frac{D_f f}{Dt} = \frac{\partial f}{\partial t} + \mathbf{U}_f \cdot \nabla f \quad \frac{D_s f}{Dt} = \frac{\partial f}{\partial t} + \mathbf{U}_s \cdot \nabla f \quad (101)$$

we use some definition following [16] as below:

$$-\frac{1}{V} \left[ \frac{\partial V_f}{\partial p} \right] \equiv \kappa_f \quad \text{isothermal compressibility of fluid} \quad (102)$$

$$\frac{1}{V} \left[ \frac{\partial V_f}{\partial T} \right] \equiv \alpha_f \quad \text{constant pressure thermal expansivity of fluid} \quad (103)$$

716 Then, the rate of volume with incompressible solid grains are calculated as  
 717 belowbelow:

$$\frac{1}{V} \frac{D_f V_f}{Dt} = \frac{1}{V} \left( \left[ \frac{\partial V_f}{\partial p} \right] \frac{D_f P_{eq}}{Dt} + \left[ \frac{\partial V_f}{\partial T_f} \right] \frac{D_f T_f}{Dt} \right) = \frac{1}{V} \left( -\kappa_f \frac{D_f P_{eq}}{Dt} + \alpha_f \frac{D_f T_f}{Dt} \right) \quad (104)$$

718 *Evolution of porosity*

719 Solving the solid mass balance equation (4) with the definition of solid  
 720 mass in equation (2), it leads to the rate of porosity as belowbelows:

$$\frac{D_s m_s}{Dt} = \frac{D_s(\phi_s \rho_s V)}{Dt} = \rho_s V \frac{D_s \phi_s}{Dt} + \phi_s V \frac{D_s \rho_s}{Dt} + \phi_s \rho_s \frac{D_s V}{Dt} = 0 \quad (105)$$

721 The soil grains are assumed to be incompressible, therefore, term 2 in the  
 722 right hand side is zero. leading to:

$$V \frac{D_s \phi_s}{Dt} + \phi_s \frac{D_s V}{Dt} = 0 \quad (106)$$

723 Dividing all terms with  $V$  with the equation  $\frac{1}{V} \frac{D_s V}{Dt} = \nabla \cdot \mathbf{U}_s$ , it leads to:

$$\frac{D_s n}{Dt} = \frac{\partial n}{\partial t} + \mathbf{U}_s \cdot \nabla n = \phi_s \nabla \cdot \mathbf{U}_s \quad (107)$$

724 *Momentum conservation*

725 The linear momentum balance equationequations for the fluid phases  
 726 based on mixture theory isare:

$$\frac{1}{V} \frac{D_f(m_f \mathbf{U}_f)}{Dt} = \nabla \cdot (-\phi_f p_f \mathbf{I}) + \nabla \cdot \boldsymbol{\tau}_f + \bar{\rho}_f \mathbf{b} + \sum \mathbf{f}_d + \mathbf{f}_b \quad (108)$$

728 On the right hand sand, the first term is the divergence of partial fluid phase  
 729 stress, the third term is the body force, the fourth term is the drag force  
 730 (momentum exchange) and the fifth term is the buoyant force described in  
 731 [29] for the immiscible mixtures. The buoyant force is in the form asbelows:

$$\mathbf{f}_b = \boldsymbol{\sigma}_f \nabla(n) \quad (109)$$

733 As a result, the linear momentum balance equationequations for the fluid  
 734 phases beeomesbecome as:

$$\frac{1}{V} \frac{D_f(m_f \mathbf{U}_f)}{Dt} = \frac{1}{V} \left[ \frac{\partial(m_f \mathbf{U}_f)}{\partial t} + \nabla \cdot (m_f \mathbf{U}_f \mathbf{U}_f) \right] = -\phi_f \nabla p_f + \nabla \cdot \boldsymbol{\tau}_f + \bar{\rho}_f \mathbf{b} + \sum \mathbf{f}_d \quad (110)$$

735 The Reynolds stress component can be included in the term  $\boldsymbol{\tau}_f$  to consider the  
 736 turbulent effects if needed. To derive the linear momentum balance equation

<sup>737</sup> for the solid phase, we begin with the linear momentum balance equation for  
<sup>738</sup> the mixture as:

$$\frac{1}{V} \frac{D_f(m_f \mathbf{U}_f)}{Dt} + \frac{1}{V} \frac{D_s(m_s \mathbf{U}_s)}{Dt} = \nabla \cdot (\boldsymbol{\sigma}) + \bar{\rho}_f \mathbf{b} + \bar{\rho}_s \mathbf{b} \quad (111)$$

<sup>739</sup> Combining Terzaghi's equation (3) and subtracting both sides with equation  
<sup>740</sup> (110), we obtain the linear momentum balance ~~equation~~-equations for the  
<sup>741</sup> solid phase as:

$$\frac{1}{V} \frac{D_s(m_s \mathbf{U}_s)}{Dt} = \nabla \cdot (\boldsymbol{\sigma}') - \phi_s \nabla p_f + \bar{\rho}_s \mathbf{b} - \sum \mathbf{f}_d + \sum \mathbf{f}_{fric} \quad (112)$$

<sup>742</sup> Here the  $\mathbf{f}_{fric}$  stems from the soil-structure interaction following the contact  
<sup>743</sup> law between the soil/structure ~~interaces~~interfaces.

#### <sup>744</sup> Energy conservation

<sup>745</sup> We adopt the general form of the total energy balance equation for the  
<sup>746</sup> porous media from [30], the total energy balance equations for the fluid phases  
<sup>747</sup> are:

$$\frac{1}{V} \frac{D_f(m_f(e_f + 0.5 \mathbf{U}_f^2))}{Dt} = \nabla \cdot (-np_f \mathbf{I}) \cdot \mathbf{U}_f + \nabla \cdot \mathbf{q}_f + (\bar{\rho}_f \mathbf{b}) \cdot \mathbf{U}_f + \sum \mathbf{f}_d \cdot \mathbf{U}_f + \sum q_{sf} \quad (113)$$

<sup>748</sup> Applying the product rule  $D(m\mathbf{U}^2) = D(m\mathbf{U} \cdot \mathbf{U}) = 2\mathbf{U} \cdot D(m\mathbf{U})$ , the left  
<sup>749</sup> hand side of equation (113) becomes:

$$\frac{1}{V} \frac{D_f(m_f(e_f + 0.5 \mathbf{U}_f^2))}{Dt} = \frac{1}{V} \frac{D_f(m_f e_f)}{Dt} + \frac{1}{V} \frac{D_f(m_f \mathbf{U}_f)}{Dt} \cdot \mathbf{U}_f \quad (114)$$

<sup>751</sup> Combining equations (110), (113), (114), we obtain the final form of the  
<sup>752</sup> internal energy balance equation for the fluid phases as:

$$\frac{1}{V} \frac{D_f(m_f e_f)}{Dt} = \frac{1}{V} \left[ \frac{\partial(m_f e_f)}{\partial t} + \nabla \cdot (m_f e_f \mathbf{U}_f) \right] = \bar{\rho}_f p_f \frac{D_f v_f}{Dt} + \nabla \cdot \mathbf{q}_f + \sum q_{sf} \quad (115)$$

<sup>753</sup> On the right hand side, the terms include the average pressure-volume work,  
<sup>754</sup> the average viscous dissipation, the thermal transport and the energy ex-  
<sup>755</sup> change between solid and fluid respectively. The heat flux is  $\mathbf{q}_f = \bar{\rho}_f \beta_f \nabla T_f$   
<sup>756</sup> with  $\beta_f$  being the thermal conductivity coefficient. To derive the internal  
<sup>757</sup> energy balance equation for the solid phase, we introduce the rate of the

758 internal energy for the thermoelastic materials as a function of elastic strain  
 759 tensor  $\boldsymbol{\epsilon}_s^e$  and temperature  $T_s$  as belows:

$$\frac{m_s}{V} \frac{D_s(e_s)}{Dt} = \boldsymbol{\sigma}' : \frac{D_s(\boldsymbol{\epsilon}_s^e)}{Dt} + \frac{D_s(e_s)}{D_s(T_s)} \frac{D_s(T_s)}{Dt} = \boldsymbol{\sigma}' : \frac{D_s(\boldsymbol{\epsilon}_s^e)}{Dt} + c_v \frac{D_s(T_s)}{Dt} \quad (116)$$

760  $c_v$  is the specific heat at the constant volume of the solid materials. The total  
 761 energy balance equation for the mixture based on [30] can be written as:

$$\begin{aligned} \frac{1}{V} \frac{D_f(m_f(e_f + 0.5\mathbf{U}_f^2))}{Dt} + \frac{1}{V} \frac{D_s(m_s(e_s + 0.5\mathbf{U}_s^2))}{Dt} &= \nabla \cdot (-\phi_f p_f \mathbf{I}) \cdot \mathbf{U}_f \\ &+ \nabla \cdot (\boldsymbol{\sigma}' - \phi_s p_f \mathbf{I}) \cdot \mathbf{U}_s + (-\phi_f p_f \mathbf{I}) : \nabla \mathbf{U}_f + \boldsymbol{\sigma}' : \nabla \mathbf{U}_s \\ &+ (\bar{\rho}_f \mathbf{b}) \cdot \mathbf{U}_f + (\bar{\rho}_s \mathbf{b}) \cdot \mathbf{U}_s + \nabla \cdot \mathbf{q}_f + \nabla \cdot \mathbf{q}_s + \sum \mathbf{f}_d \cdot (\mathbf{U}_f - \mathbf{U}_s) \end{aligned} \quad (117)$$

763 Subtracting equation (117), (116) to equations (113) and (112), we obtained  
 764 the internal energy balance equation for solid phase as:

$$\boldsymbol{\sigma}' : \frac{D_s(\boldsymbol{\epsilon}_s^e)}{Dt} + \frac{m_s}{V} c_v \frac{D_s(T_s)}{Dt} = \Delta W_s + \Delta W_{friction} + \nabla \cdot \mathbf{q}_s - \sum q_{sf} \quad (118)$$

765 On the right hand side, the terms include the work rate from frictional sliding  
 766 between solid materials  $\Delta W_{friction}$ , thermal transport and energy exchange  
 767 between solid and fluid respectively. The heat flux is  $\mathbf{q}_s = \bar{\rho}_s \beta_s \nabla T_s$  with  $\beta_s$   
 768 being the thermal conductivity of the solid materials, the mechanical work  
 769 rate  $\Delta W_s = \boldsymbol{\sigma}' : \frac{D_s(\boldsymbol{\epsilon}_s^e)}{Dt} = \boldsymbol{\sigma}' : (\frac{D_s(\boldsymbol{\epsilon}_s^e)}{Dt} + \frac{D_s(\boldsymbol{\epsilon}_s^p)}{Dt})$  computed from the constitutive  
 770 model with  $\boldsymbol{\epsilon}_s^p$  is the plastic strain tensor, . By subtracting the term  $\boldsymbol{\sigma}' : \frac{D_s(\boldsymbol{\epsilon}_s^e)}{Dt}$ ,  
 771 we get the final form of the energy balance equation as:

$$\frac{m_s}{V} c_v \frac{D_s(T_s)}{Dt} = \boldsymbol{\sigma}' : \frac{D_s(\boldsymbol{\epsilon}_s^p)}{Dt} + \Delta W_{friction} + \nabla \cdot \mathbf{q}_s - \sum q_{sf} \quad (119)$$

### 772 Advanced Fluid Pressure

773 The discretization of the pressure equation begins with the Lagrangian  
 774 face-centered cell face velocity and the equation for the pressure as:

$$\bar{\rho}_{f,FC} \frac{\mathbf{U}_{f,FC}^{n+1} - \mathbf{U}_{f,FC}^n}{dt} = n \nabla^{FC} P_{\textcolor{red}{fc}\textcolor{blue}{f,c}}^{n+1} + \bar{\rho}_{f,FC} \mathbf{b} \quad (120)$$

775

$$\kappa \frac{dP}{dt} = \nabla^c \cdot \mathbf{U}_{f,FC}^{n+1} \quad (121)$$

776 The divergence of the equation (120) with  $\nabla \cdot \mathbf{b} = 0$  is:

$$\nabla^c \cdot \mathbf{U}_{f,FC}^{n+1} - \nabla^c \cdot \mathbf{U}_{f,FC}^n = \nabla^c \frac{\Delta t}{\rho_{f,FC}^n} \cdot \nabla^{FC} (P_{fc,fc}^n + \Delta P_{fc,fc}^n) \quad (122)$$

777 To solve this equation, we define the ~~face-centered-cell face~~ intermediate  
778 velocity  $\mathbf{U}_{f,FC}^*$  as:

$$\bar{\rho}_{f,FC} \frac{\mathbf{U}_{f,FC}^* - \mathbf{U}_{f,FC}^n}{\Delta t} = n \nabla^{FC} P_{fc,fc}^n + \bar{\rho}_{f,FC} \mathbf{b} \quad (123)$$

779 The divergence of the equation (123) is:

$$\nabla^c \cdot \mathbf{U}_{f,FC}^* - \nabla^c \cdot \mathbf{U}_{f,FC}^n = \nabla^c \frac{\Delta t}{\rho_{f,FC}^n} \cdot \nabla^{FC} P_{fc,fc}^n \quad (124)$$

780 Combining equations (121, 122, 124), it leads to:

$$\left( \kappa - \nabla^c \frac{\Delta t}{\rho_{f,FC}^n} \cdot \nabla^{FC} \right) \Delta P_{fc}^n = -\nabla^c \cdot \mathbf{U}_{f,FC}^* \quad (125)$$

781 When the fluid is incompressible,  $\kappa$  approaches to zero and the equation  
782 (125) becomes the Poisson's equation for the incompressible fluid flow.

783 *Momentum and Energy exchange with an implicit solver*

784 Considering the fluid momentum balance equation as:

$$(m\mathbf{U})_{f,FC}^{n+1} = (m\mathbf{U})_{f,FC}^n - \Delta t (Vn \nabla^{FC} P_{fc,fc}^n + m_f \mathbf{b}) + VK \Delta t (\mathbf{U}_{s,FC}^{n+1} - \mathbf{U}_{f,FC}^{n+1}) \quad (126)$$

785 Assuming And assuming  $m_{f,FC}^{n+1} = m_{f,FC}^n$  we get, we get:

$$\mathbf{U}_{f,FC}^{n+1} = \mathbf{U}_{f,FC}^n - \Delta t \left( \frac{\nabla^{FC} P_{fc}^n}{\rho_{f,FC}^n} + \mathbf{b} \right) + \frac{\Delta t K}{\rho_{f,FC}^n} (\mathbf{U}_{s,FC}^{n+1} - \mathbf{U}_{f,FC}^{n+1}) \quad (127)$$

786 As defined in the section 'Advanced Fluid Pressure', the ~~face-centered-cell~~  
787 ~~face~~ intermediate fluid velocity  $\mathbf{U}_{f,FC}^* = \Delta t (\nabla^{FC} P_{fc}^n / \rho_{f,FC}^n + \mathbf{b})$  leading to is  
788 computed as:

$$\mathbf{U}_{f,FC}^{n+1} = \mathbf{U}_{f,FC}^* + \frac{\Delta t K}{\rho_{f,FC}^n} (\mathbf{U}_{s,FC}^{n+1} - \mathbf{U}_{f,FC}^{n+1}) \quad (128)$$

789 Considering the solid momentum balance equation as:

$$(m\mathbf{U})_{s,FC}^{n+1} = (m\mathbf{U})_{s,FC}^n - \Delta t(V\nabla^{FC} \cdot \boldsymbol{\sigma}'^n - V(1-n)\nabla^{FC}P_{fc,fc}^n + m_s\mathbf{b}) - VK\Delta t(\mathbf{U}_{s,FC}^{n+1} - \mathbf{U}_{f,FC}^{n+1}) \quad (129)$$

790 We define the face-centered cell face intermediate solid velocity as  $\mathbf{U}_{s,FC}^* = \Delta t(\nabla^{FC} \cdot \boldsymbol{\sigma}_c'^n / \bar{\rho}_{s,FC} - \nabla^{FC}P_{f,fc}^n / \rho_s + \mathbf{b})$   
 791 leading to  $\mathbf{U}_{s,FC}^* = \Delta t(\nabla^{FC} \cdot \boldsymbol{\sigma}_c'^n / \bar{\rho}_{s,FC} - \nabla^{FC}P_{f,fc}^n / \rho_s + \mathbf{b})$  leading to:

$$\mathbf{U}_{s,FC}^{n+1} = \mathbf{U}_{s,FC}^* - \frac{\Delta t K}{\bar{\rho}_{s,FC}^n} (\mathbf{U}_{s,FC}^{n+1} - \mathbf{U}_{f,FC}^{n+1}) \quad (130)$$

792 Combining equation (128) and (130) we get:

$$\begin{aligned} \mathbf{U}_{f,FC}^* + \Delta\mathbf{U}_{f,FC} &= \mathbf{U}_{f,FC}^* + \frac{\Delta t K}{\bar{\rho}_{f,FC}^n} (\mathbf{U}_{s,FC}^* + \Delta\mathbf{U}_{s,FC} - \mathbf{U}_{f,FC}^* - \Delta\mathbf{U}_{f,FC}) \\ \mathbf{U}_{s,FC}^* + \Delta\mathbf{U}_{s,FC} &= \mathbf{U}_{s,FC}^* - \frac{\Delta t K}{\bar{\rho}_{s,FC}^n} (\mathbf{U}_{s,FC}^* + \Delta\mathbf{U}_{s,FC} - \mathbf{U}_{f,FC}^* - \Delta\mathbf{U}_{f,FC}) \end{aligned} \quad (131)$$

793 Rearranging the equation (131), it leads to the linear system of equations as  
 794 belows:

$$\begin{vmatrix} (1 + \beta_{12,FC}) & -\beta_{12,FC} \\ -\beta_{21,FC} & (1 + \beta_{21,FC}) \end{vmatrix} \begin{vmatrix} \Delta\mathbf{U}_{f,FC} \\ \Delta\mathbf{U}_{s,FC} \end{vmatrix} = \begin{vmatrix} \beta_{12,FC}(\mathbf{U}_{s,FC}^* - \mathbf{U}_{f,FC}^*) \\ \beta_{21,FC}(\mathbf{U}_{f,FC}^* - \mathbf{U}_{s,FC}^*) \end{vmatrix}$$

795 Solving this linear equations with  $\beta_{12,FC} = (\Delta t K) / \bar{\rho}_{f,FC}^n$  and  $\beta_{21,FC} = (\Delta t K) / \bar{\rho}_{s,FC}^n$  with K is the momentum exchange coefficient. Similar derivation can be performed to computed the cell-center velocity increment leading to:

$$\begin{vmatrix} (1 + \beta_{12c}) & -\beta_{12c} \\ -\beta_{21c} & (1 + \beta_{21c}) \end{vmatrix} \begin{vmatrix} \Delta\mathbf{U}_{fc,fc} \\ \Delta\mathbf{U}_{sc} \end{vmatrix} = \begin{vmatrix} \beta_{12c}(\mathbf{U}_{sc}^* - \mathbf{U}_{fc,fc}^*) \\ \beta_{21c}(\mathbf{U}_{fc,fc}^* - \mathbf{U}_{sc}^*) \end{vmatrix}$$

799 with  $\beta_{12c} = (\Delta t K) / \bar{\rho}_{fc}^n$   $\beta_{12c} = (\Delta t K) / \bar{\rho}_{fc}^n$  and  $\beta_{21c} = (\Delta t K) / \bar{\rho}_{sc}^n$  and the  
 800 cell-centered intermediate velocity can be calculated by:

$$\begin{aligned} \mathbf{U}_{fc,fc}^* &= \mathbf{U}_{fc,fc}^n + \Delta t \left( -\frac{\nabla P_{fc}^{n+1}}{\bar{\rho}_{fc}^n} \frac{\nabla P_{f,fc}^{n+1}}{\bar{\rho}_{f,fc}^n} + \frac{\nabla \cdot \boldsymbol{\tau}_{fc}^n}{\bar{\rho}_{fc}^n} \frac{\nabla \cdot \boldsymbol{\tau}_{f,fc}^n}{\bar{\rho}_{f,fc}^n} + \mathbf{b} \right) \\ \mathbf{U}_{sc}^* &= \mathbf{U}_{sc}^n + \Delta t \left( \frac{\nabla \cdot \boldsymbol{\sigma}_c'^n}{\bar{\rho}_{sc}^n} - \frac{\nabla P_{fc}^{n+1}}{\bar{\rho}_s} \frac{\nabla P_{f,fc}^{n+1}}{\bar{\rho}_s} + \mathbf{b} \right) \end{aligned} \quad (132)$$

801 For generalize multi materials i,j = 1:N, the linear equations is in the form  
802 as:

$$\begin{vmatrix} (1 + \beta_{ij}) & -\beta_{ij} \\ -\beta_{ji} & (1 + \beta_{ji}) \end{vmatrix} \begin{vmatrix} \Delta \mathbf{U}_i \\ \Delta \mathbf{U}_j \end{vmatrix} = \begin{vmatrix} \beta_{ij}(\mathbf{U}_i^* - \mathbf{U}_j^*) \\ \beta_{ji}(\mathbf{U}_j^* - \mathbf{U}_i^*) \end{vmatrix}$$

803 Similar approach applied for the ernergy exchange term leading to:

$$\begin{vmatrix} (1 + \eta_{ij}) & -\eta_{ij} \\ -\eta_{ji} & (1 + \eta_{ji}) \end{vmatrix} \begin{vmatrix} \Delta T_i \\ \Delta T_j \end{vmatrix} = \begin{vmatrix} \eta_{ij}(T_i^n - T_j^n) \\ \eta_{ji}(T_j^n - T_i^n) \end{vmatrix}$$

804 with  $\eta$  is the energy exchange coefficient.

## 805 References

- 806 [1] D. Yuk, S. Yim, P.-F. Liu, Numerical modeling of submarine mass-  
807 movement generated waves using RANS model, Computers and Geo-  
808 sciences 32 (7) (2006) 927–935. doi:10.1016/j.cageo.2005.10.028.  
809 URL <https://doi.org/10.1016/j.cageo.2005.10.028>
- 810 [2] S. Glimsdal, J.-S. L'Heureux, C. B. Harbitz, F. Løvholt, The 29th jan-  
811 uary 2014 submarine landslide at statland, norway—landslide dynamics,  
812 tsunami generation, and run-up, Landslides 13 (6) (2016) 1435–1444.  
813 doi:10.1007/s10346-016-0758-7.  
814 URL <https://doi.org/10.1007/s10346-016-0758-7>
- 815 [3] S. Abadie, D. Morichon, S. Grilli, S. Glockner, Numerical sim-  
816 ulation of waves generated by landslides using a multiple-fluid  
817 navier–stokes model, Coastal Engineering 57 (9) (2010) 779–794.  
818 doi:10.1016/j.coastaleng.2010.03.003.  
819 URL <https://doi.org/10.1016/j.coastaleng.2010.03.003>
- 820 [4] M. Rauter, S. Viroulet, S. S. Gylfadóttir, W. Fellin, F. Løvholt, Granular  
821 porous landslide tsunami modelling – the 2014 lake askja flank collapse,  
822 Nature Communications 13 (1) (Feb. 2022). doi:10.1038/s41467-022-  
823 28296-7.  
824 URL <https://doi.org/10.1038/s41467-022-28296-7>
- 825 [5] Q.-A. Tran, W. Sołowski, Generalized interpolation material point  
826 method modelling of large deformation problems including strain-  
827 rate effects – application to penetration and progressive fail-  
828 ure problems, Computers and Geotechnics 106 (2019) 249–265.

- 829 doi:10.1016/j.compgeo.2018.10.020.  
830 URL <https://doi.org/10.1016/j.compgeo.2018.10.020>
- 831 [6] T. Capone, A. Panizzo, J. J. Monaghan, SPH modelling of water  
832 waves generated by submarine landslides, *Journal of Hydraulic Research*  
833 48 (sup1) (2010) 80–84. doi:10.1080/00221686.2010.9641248.  
834 URL <https://doi.org/10.1080/00221686.2010.9641248>
- 835 [7] X. Zhang, E. Oñate, S. A. G. Torres, J. Bleyer, K. Krabbenhoft, A  
836 unified lagrangian formulation for solid and fluid dynamics and its possi-  
837 bility for modelling submarine landslides and their consequences, *Computer  
838 Methods in Applied Mechanics and Engineering* 343 (2019) 314–  
839 338. doi:10.1016/j.cma.2018.07.043.  
840 URL <https://doi.org/10.1016/j.cma.2018.07.043>
- 841 [8] R. Dey, B. C. Hawlader, R. Phillips, K. Soga, Numerical modelling  
842 of submarine landslides with sensitive clay layers, *Géotechnique* 66 (6)  
843 (2016) 454–468. doi:10.1680/jgeot.15.p.111.  
844 URL <https://doi.org/10.1680/jgeot.15.p.111>
- 845 [9] S. Bandara, K. Soga, Coupling of soil deformation and pore fluid flow  
846 using material point method, *Computers and Geotechnics* 63 (2015)  
847 199–214. doi:10.1016/j.compgeo.2014.09.009.  
848 URL <https://doi.org/10.1016/j.compgeo.2014.09.009>
- 849 [10] A. P. Tampubolon, T. Gast, G. Klár, C. Fu, J. Teran, C. Jiang,  
850 K. Museth, Multi-species simulation of porous sand and water  
851 mixtures, *ACM Transactions on Graphics* 36 (4) (2017) 1–11.  
852 doi:10.1145/3072959.3073651.  
853 URL <https://doi.org/10.1145/3072959.3073651>
- 854 [11] A. S. Baumgarten, K. Kamrin, A general constitutive model for dense,  
855 fine-particle suspensions validated in many geometries, *Proceedings  
856 of the National Academy of Sciences* 116 (42) (2019) 20828–20836.  
857 doi:10.1073/pnas.1908065116.  
858 URL <https://doi.org/10.1073/pnas.1908065116>
- 859 [12] Q.-A. Tran, W. Sołowski, Temporal and null-space filter for the ma-  
860 terial point method, *International Journal for Numerical Methods in*

- 861      Engineering 120 (3) (2019) 328–360. doi:10.1002/nme.6138.  
862      URL <https://doi.org/10.1002/nme.6138>
- 863 [13] X. Zheng, F. Pisanò, P. J. Vardon, M. A. Hicks, An explicit stabilised  
864 material point method for coupled hydromechanical problems in two-  
865 phase porous media, Computers and Geotechnics 135 (2021) 104112.  
866 doi:10.1016/j.compgeo.2021.104112.  
867 URL <https://doi.org/10.1016/j.compgeo.2021.104112>
- 868 [14] Q. A. Tran, W. Sołowski, M. Berzins, J. Guilkey, A convected particle  
869 least square interpolation material point method, International Journal  
870 for Numerical Methods in Engineering 121 (6) (2019) 1068–1100.  
871 doi:10.1002/nme.6257.  
872 URL <https://doi.org/10.1002/nme.6257>
- 873 [15] J.-S. Chen, M. Hillman, S.-W. Chi, Meshfree methods: Progress made  
874 after 20 years, Journal of Engineering Mechanics 143 (4) (Apr. 2017).  
875 doi:10.1061/(asce)em.1943-7889.0001176.  
876 URL [https://doi.org/10.1061/\(asce\)em.1943-7889.0001176](https://doi.org/10.1061/(asce)em.1943-7889.0001176)
- 877 [16] B. A. Kashiwa, A multifield model and method for fluid-structure in-  
878 teraction dynamics, Tech. Rep. LA-UR-01-1136, Los Alamos National  
879 Laboratory (2001).
- 880 [17] J. Guilkey, T. Harman, B. Banerjee, An eulerian–lagrangian  
881 approach for simulating explosions of energetic devices,  
882 Computers and Structures 85 (11) (2007) 660 – 674.  
883 doi:<https://doi.org/10.1016/j.compstruc.2007.01.031>.  
884 URL <http://www.sciencedirect.com/science/article/pii/S0045794907000429>
- 885 [18] A. S. Baumgarten, B. L. Couchman, K. Kamrin, A coupled finite volume  
886 and material point method for two-phase simulation of liquid–sediment  
887 and gas–sediment flows, Computer Methods in Applied Mechanics and  
888 Engineering 384 (2021) 113940. doi:10.1016/j.cma.2021.113940.  
889 URL <https://doi.org/10.1016/j.cma.2021.113940>
- 890 [19] S. Bardenhagen, J. Guilkey, K. Roessig, J. Brackbill, W. Witzel,  
891 J.C.Foster, An improved contact algorithm for the material point  
892 method and application to stress propagation in granular material,

- 893 CMES-Computer Modeling in Engineering and Sciences 2 (2001) 509–  
894 522. doi:10.3970/cmes.2001.002.509.
- 895 [20] J. A. M. K. R. Beetstra, M. A. van der Hoef, Drag force of intermediate  
896 reynolds number flow past mono- and bidisperse arrays of spheres,  
897 Fluid Mechanics and Transport Phenomena 53 (2) (2007) 489 – 501.  
898 doi:<https://doi.org/10.1002/aic.11065>.
- 899 [21] R. W. Stewart, The air-sea momentum exchange, Boundary-Layer Me-  
900 teorology 6 (1-2) (1974) 151–167. doi:10.1007/bf00232481.  
901 URL <https://doi.org/10.1007/bf00232481>
- 902 [22] S. G. Bardenhagen, E. M. Kober, The generalized interpolation material  
903 point method, Computer Modeling in Engineering and Sciences 5 (2004)  
904 477–496. doi:10.1016/j.compgeo.2021.104199.  
905 URL <https://doi.org/10.3970/cmes.2004.005.477>
- 906 [23] S. G. Amiri, E. Taheri, A. Lavasan, A hybrid finite element model for  
907 non-isothermal two-phase flow in deformable porous media, Computers  
908 and Geotechnics 135 (2021) 104199. doi:10.1016/j.compgeo.2021.104199.  
909 URL <https://doi.org/10.1016/j.compgeo.2021.104199>
- 910 [24] S. A. R. C. Mariotti;, P. Heinrich, Numerical simulation of sub-  
911 marine landslides and their hydraulic effects, Journal of Wa-  
912 terway, Port, Coastal, and Ocean Engineering 123 (4) (1997).  
913 doi:[https://doi.org/10.1061/\(ASCE\)0733-950X\(1997\)123:4\(149\).](https://doi.org/10.1061/(ASCE)0733-950X(1997)123:4(149).)
- 914 [25] A. Alsardi, A. Yerro, Runout Modeling of Earthquake-Triggered  
915 Landslides with the Material Point Method, pp. 21–31.  
916 arXiv:<https://ascelibrary.org/doi/pdf/10.1061/9780784483428.003>,  
917 doi:10.1061/9780784483428.003.  
918 URL <https://ascelibrary.org/doi/abs/10.1061/9780784483428.003>
- 919 [26] H. N., O. A., B. H. H., R. P., R. Fukagawa, Seismic slope failuremod-  
920 elling using the mesh-free sph method, International Journal of Geomate  
921 (2013) 660–665.
- 922 [27] T. Bhandari, F. Hamad, C. Moormann, K. Sharma,  
923 B. Westrich, Numerical modelling of seismic slope failure us-  
924 ing mpm, Computers and Geotechnics 75 (2016) 126–134.

- 925                   doi:<https://doi.org/10.1016/j.compgeo.2016.01.017>.  
926                   URL <https://www.sciencedirect.com/science/article/pii/S0266352X16000264>
- 927 [28] D. Muir Wood, Soil behaviour and critical state soil mechanics, Cam-  
928                   bridge University Press, United Kingdom, 1990.
- 929 [29] D. Drumheller, On theories for reacting immiscible mixtures, Inter-  
930                   national Journal of Engineering Science 38 (3) (2000) 347 – 382.  
931                   doi:[https://doi.org/10.1016/S0020-7225\(99\)00047-6](https://doi.org/10.1016/S0020-7225(99)00047-6).  
932                   URL <http://www.sciencedirect.com/science/article/pii/S0020722599000476>
- 933 [30] S. Hassanzadeh, Derivation of basic equations of mass transport in  
934                   porous media, part1: Macroscopic balance laws, Advances in Wa-  
935                   ter Resources 9 (1986) 196–206. doi:[https://doi.org/10.1016/0309-1708\(86\)90024-2](https://doi.org/10.1016/0309-1708(86)90024-2).